New line positions analysis of the 2 ν 1 and ν 1 + ν 3 bands of NO 2 at 3637.848 and 2906.070 cm −1

Agnès Perrin, L. Manceron, F. Kwabia Tchana

TMPH1711235 VOL 00, ISS 00

New line positions analysis of the $2\nu_1$ and $\nu_1 + \nu_3$ bands of NO_2 at 3637.848 and 2906.070 cm^{-1}

Agnès Perrin, L. Manceron, and F. Kwabia Tchana

QUERY SHEET

This page lists questions we have about your paper. The numbers displayed at left are hyperlinked to the location of the query in your paper.

The title and author names are listed on this sheet as they will be published, both on your paper and on the Table of Contents. Please review and ensure the information is correct and advise us if any changes need to be made. In addition, please review your paper as a whole for typographical and essential corrections.

Your PDF proof has been enabled so that you can comment on the proof directly using Adobe Acrobat. For further information on marking corrections using Acrobat, please visit http://journalauthors.tandf.co.uk/production/acrobat.asp; https://authorservices.taylorandfrancis.com/how-to-correct-proofs-with-adobe/

The CrossRef database (www.crossref.org/) has been used to validate the references.

AUTHOR QUERIES

QUERY NO.	QUERY DETAILS
Q1	Please check whether the affiliations have been set correctly.
Q2	Please note that the journal allows 3–5 keywords. Please edit keywords accordingly.
Q3	Please note that the Funding section has been created by summarising information given in your acknowledgements. Please correct if this is inaccurate.
Q4	The funding information provided (CNRS) has been checked against the Open Funder Registry and we found a partial match with "CNRS". Please check and resupply the funding details.
Q5	An opening quotation mark seems to be missing following "... to assess the CO_2 content". Please indicate where it should be placed.
Q6	Equations have renumbered. Please confirm.
Q7	The disclosure statement has been inserted. Please correct if this is inaccurate.
Q8	The reference [28] is listed in the references list but is not cited in the text. Please either cite the reference or remove it from the references list.
Q9	The reference [29] is listed in the references list but is not cited in the text. Please either cite the reference or remove it from the references list.
Q10	The reference [31] is listed in the references list but is not cited in the text. Please either cite the reference or remove it from the references list.

MOLECULAR PHYSICS
https://doi.org/10.1080/00268976.2019.1711235

Taylor & Francis
Taylor & Francis Group

HRMS 2019

New line positions analysis of the $2\nu_1$ and $\nu_1 + \nu_3$ bands of NO_2 at 3637.848 and 2906.070 cm^{-1}

Agnès Perrin[a], L. Manceron[b,c] and F. Kwabia Tchana[d]

[a]Laboratoire de Météorologie Dynamique/IPSL, UMR CNRS 8539, Ecole Polytechnique, Université Paris-Saclay, Palaiseau, France; [b]Ligne AILES, Synchrotron SOLEIL, L'Orme des Merisiers, Gif-sur-Yvette, France; [c]MONARIS, UMR 8233, CNRS, Sorbonne Université, Paris, France; [d]Laboratoire Interuniversitaire des Systèmes Atmosphériques (LISA), UMR CNRS 7583, Institut Pierre Simon Laplace (IPSL), Université de Paris et Université Paris Est Créteil, Créteil, France

ABSTRACT

Using a high-resolution Fourier transform spectrum recorded at SOLEIL for a rather large value of the (pressure × path length) product a new investigation of the very weak $2\nu_1$ absorption band of nitrogen dioxide, located at 2627.377 cm^{-1} was performed, together with an extension up to higher N and K_a values of a previous investigation of the strong $\nu_1 + \nu_3$ band [J.-Y. Mandin, V. Dana, A. Perrin, J.-M. Flaud, C. Camy-Peyret, L. Régalia and A. Barbe, J. Mol. Spectrosc. 181, 379 (1997)]. The $2\nu_1$ lines proved to be perturbed by local vibration–rotation resonances which couple the (2,0,0) energy levels with those of the (1,2,0) and (1,0,1) states. Also the (1,0,1) energy levels are also coupled by a C-type Coriolis resonance with those of the (1,2,0) and (2,0,0) energy levels. The final energy levels calculation involves six interacting states of NO_2, {(2,0,0), (1,2,0), (1,0,1), (0,0,2), (0,4,0), (0,0,2)}. An estimation of line intensities parameters was performed for the very weak $2\nu_1$ band. Finally a list of line parameters (positions, intensities and shapes) for the $2\nu_1$, $\nu_1 + 2\nu_2$ and $\nu_1 + \nu_3$ bands of NO_2, was generated and is now included in the GEISA database (https://geisa.aeris-data.fr/).

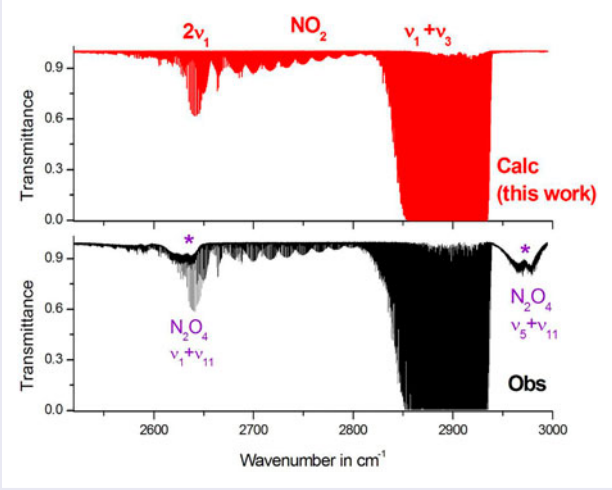

ARTICLE HISTORY
Received 17 October 2019
Accepted 13 December 2019

KEYWORDS
$^{14}N^{16}O_2$; nitrogen dioxide; Fourier transform spectroscopy; electron spin-rotation resonances; Coriolis resonances; Fermi resonances; line positions; line intensities; 3.8 and 3.44 µm regions; GEISA

1. Introduction

Nitrogen dioxide ($^{14}N^{16}O_2$) is an asymmetric rotor with an unpaired electron. In the infrared region, the electron spin-rotation interaction causes a doublet structure, usually observable, while in the microwave and far-infrared spectral regions, the hyperfine structure due to the $I = 1$ nuclear spin is observable [1,2].

In addition, rovibrational interactions are to be accounted for in order to reproduce the measured line positions and intensities. Starting with the first triad of

CONTACT Agnès Perrin agnes.perrin@lmd.polytechnique.fr Laboratoire de Météorologie Dynamique/IPSL, UMR CNRS 8539, Ecole Polytechnique, Université Paris-Saclay, RD36, 91128 Palaiseau Cedex, France

Supplemental data for this article can be accessed here. https://doi.org/10.1080/00268976.2019.1711235

Table 1. Positions and relative band intensities of the $2\nu_1$, $\nu_1+2\nu_2$, $\nu_1+\nu_3$, $2\nu_2+\nu_3$, $4\nu_2$, and $2\nu_3$ bands of $^{14}N^{16}O_2$.

Band	$2\nu_1$	$\nu_1+2\nu_2$	$\nu_1+\nu_3$	$4\nu_2$	$2\nu_2+\nu_3$	$2\nu_3$
Band centre	2627.37672	2805.80	2906.0706	2992.782	3092.4757	3201.4481
Type	B-type	B-type	A-type	B-type	A-type	B-type
Ratio[a]	~ 1/350	~ 1/3000	1.	~ 1/10,000	~ 1/460	~ 1/780
Ref.:	This work	[7]	[7]	[5]	[5]	[5]

[a]Caption: Ratio = Int(band)/Int($\nu_1+\nu_3$).

interacting states {(1,0,0), (0,2,0), (0,0,1)}, strong second-order C-type Coriolis resonances are coupling the spin-rotational levels of the (v_1, v_2, v_3) and (v_1, $v_2\pm2$, v_3^-+1) vibrational states. See for example our papers [3–9]. In addition, for the first triad, the (1,0,0) and (0,0,1) energy levels involving rather high K_a values ($15 \geq K_a \geq 10$) [3] are coupled through a first-order C-type Coriolis resonance. Finally, at higher energies ($E_v \geq 5984\,cm^{-1}$), additional high order vibration–rotation interactions involving vibrational states differing by a large number of vibrational quanta were identified [9].

Before going into details, one has to point out that the goal of the present study is restricted to the investigations of the $2\nu_1$, $\nu_1+\nu_3$ and $\nu_1+2\nu_2$ cold bands of $^{14}N^{16}O_2$. To perform a new investigation of the $2\nu_1$ band located at $2627.3767\,cm^{-1}$, on the low-frequency range of the significantly stronger $\nu_1+\nu_3$ band, at $2906.074\,cm^{-1}$, we recorded a Fourier transform spectrum (FTS) for a rather large (pressure × path length) product. It proved that the spectrum recorded in conditions suitable for the investigation of the $2\nu_1$ band, is almost completely saturated in the 2850–2930 cm^{-1} spectral range which corresponds to the lines involving low or medium N and K_a values of the much stronger $\nu_1+\nu_3$ band. However, by analysing the spectrum in the wings of $\nu_1+\nu_3$ spectral range or in small windows within strong lines, we could pursue up to higher N and K_a values the investigation of the $\nu_1+\nu_3$ band that we performed some years ago [7]. So the present study includes also a new investigation of the stronger $\nu_1+\nu_3$ band.

First, it is necessary to describe the status of these bands in the literature. For reasons which will become clear later in the text, this short review will also include a description of the most recent analysis of the $2\nu_2+\nu_3$, $4\nu_2$, and $2\nu_3$ band of NO_2 [5]. To help the reading of this manuscript, Table 1 gives the positions and relative band intensities of the $2\nu_1$, $\nu_1+2\nu_2$, $\nu_1+\nu_3$, $2\nu_2+\nu_3$, $4\nu_2$, and $2\nu_3$ bands.

1.1. The $2\nu_1$ band

The $2\nu_1$ B-type band was investigated at grating spectroscopy resolution by Cabana *et al.* [10]. This first investigation led to the identification of (2,0,0) spin-rotational energy levels up to $N = 57$ and $K_a = 10$. The spin-rotation effect was accounted for using a 2d order perturbation treatment [11]. No noticeable vibrational–rotational resonance was explicitly observed during the analysis. However, it proved that the (2,0,0) energy levels involving K_a values with $K_a \geq 9$ could not satisfactorily reproduced by the computation using a Watson' type rotational Hamiltonian and were therefore removed from the final computation. Also Cabana *et al.* [10] mentioned that the $2\nu_1$ band exhibits severe internal intensity anomalies. Briefly speaking, the transitions located in the low-frequency side of the $2\nu_1$ band, which corresponds to the ^PP-branch, are quite weak. Therefore about 80% of the band intensity is located on the high-frequency side of the band origin, corresponding to the Q and ^RR-branch.

1.2. The $\nu_1 \pm \nu_3$ band [7] and the $2\nu_2 \pm \nu_3$, $4\nu_2$, and $2\nu_3$ [5] interacting bands of $^{14}N^{16}O_2$

The most recent and complete investigations of the $\nu_1+\nu_3$ band and of the $2\nu_2+\nu_3$, $4\nu_2$, and $2\nu_3$ interacting bands were performed using high-resolution Fourier transform spectra recorded at high resolution ($R \sim 0.003\,cm^{-1}$) in the 2633–2970 cm^{-1} [7] and 3000–3400 cm^{-1} [5], spectral ranges, respectively. The results of the assignments (number of lines, numbers of upper state energy levels, maximum values of K_a and N) are described shortly in Table 2. During the energy level computations, both the spin-rotational interactions within each vibrational state, and the vibration–rotation interactions were explicitly accounted for. For the {(1,2,0), (1,0,1)} diad [7], the (1,2,0) $\Longleftrightarrow$ (1,0,1) C-type Coriolis resonances, although not negligible, are rather weak, and this is why no line belonging to the $\nu_1+2\nu_2$ dark band could be identified during this 1997 study [7]. On the other hand, for the $2\nu_2+\nu_3$, $4\nu_2$, and $2\nu_3$ bands, the C-type Coriolis resonances coupling (0,2,1) $\Longleftrightarrow$ (0,4,0), and (0,2,1) $\Longleftrightarrow$ (0,0,2) resonating energy levels are rather strong. This explains why numerous $4\nu_2$ band lines involving $K_a = 5$ in the (0,4,0) upper level could be observed.

In addition, a large set of individual experimental line intensities were measured during both analyses, leading

Table 2. Range of the observed energy levels and statistical analysis of the results of the energy level calculation.

	Nb of lines	Nb of levels	N max	K_a max	
(2,0,0)–(0,0,0)			52	10	Ref. [10]
(2,0,0)–(0,0,0)	2188	992	62	12	This work
(1,0,1)–(0,0,0)	856	550	75	14	This work
(1,0,1)–(0,0,0)	1228	746	55	10	Ref. [7]
Total: (1,0,1)–(0,0,0)		1296	75	14	Ref.[7] and this work
(1,2,0)–(0,0,0)	41	41	27–57	$K_a = 6$ (mainly) and $K_a = 3$ and 5	This work
(0,2,1)–(0,0,0)	970	496	49	6	Ref. [5]
(0,4,0)–(0,0,0)	76	41	27	$K'_a = 5$	Ref. [5]
(0,0,2)–(0,0,0)	1097	490	60	8	Ref. [5]

to the determination of the transition operators for the $\nu_1+\nu_3$ band [7] and of the $2\nu_2+\nu_3$, $4\nu_2$, and $2\nu_3$ [5] interacting bands. Finally, comprehensive lists of line positions and intensities for the interacting $\nu_1+2\nu_2$ and $\nu_1+\nu_3$ bands [7] and for the $2\nu_2+\nu_3$, $4\nu_2$ and $2\nu_3$ [5] interacting bands of $^{14}N^{16}O_2$ have been generated covering the 3.4 and 3.2 µm regions, respectively.

The $\nu_1+\nu_3$ band of nitrogen dioxide was also the subject of line broadening studies [12], and the list of line positions, intensities and line shape parameters generated for the $\nu_1+\nu_3$ band of $^{14}N^{16}O_2$ at 3.44 µm is now implemented in HITRAN [13] and the GEISA [14] databases. These GEISA and HITRAN line lists include also parameters belonging to the $\nu_1+\nu_2+\nu_3-\nu_2$ first hot band at 3.5 µm. Let us note that the $\nu_1+\nu_2+\nu_3$ band at 3637.8479 cm^{-1} was the subject of a recent investigation [6], leading to a better energy level prediction for the (1,1,1) upper vibrational state.

Finally, let us mention the analysis performed for the $\nu_1+\nu_3$ band for the $^{15}N^{16}O_2$ species of nitrogen dioxide at 2858.7077 cm^{-1}, which contributes to about 0.364% to the band intensity in the 3.49 µm region [15].

1.3. The recent HITEMP database

The aim of the HITEMP ('HIgh-TEMPerature molecular spectroscopic database') [16] is to model gas phase spectra for high-temperature applications. The most recent update [17] of this database involves the NO_2 molecule for the first time. For this species, a composite linelist was generated by extending the current HITRAN2016 linelist [13] using inputs from the recent NDSD-1000 [18,19] line list. For the vibrational transitions (like (1,0,1)–(0,0,0)) which are already considered in HITRAN, the NDSD-1000 has provided an extension of the current list up to the higher N and K_a values. HITEMP also includes linelists for several cold and hot bands which, up to now, are missing in the current HITRAN or GEISA databases. Indeed, only the first hot bands ($\nu_2-\nu_2$, $2\nu_2-\nu_2$, $\nu_2+\nu_3-\nu_2$, and $\nu_1+\nu_2+\nu_3-\nu_2$), are, up to now, considered in HITRAN or GEISA.

The present study uses an FT spectrum recorded in the 2400–2960 cm^{-1} spectral region for a NO_2 sample at $T = 296$ K temperature and for a large (pressure × path length) product. Therefore, the line parameters quoted in HITEMP which are missing in HITRAN and are of interest for this study are mainly those belonging either to the weak $2\nu_1$ band or to the various hot bands associated to $\nu_1+\nu_3$. However, it is clear that, in the high-frequency range of our spectrum ($\sigma \geq 2920$ cm^{-1}) which corresponds to the R-branch, the hot bands give rise to little contribution at 296 K and we do not distinguish the difference between the predictions provided by HITEMP and HITRAN or GEISA.

2. Experimental details

A high-resolution absorption spectrum of nitrogen dioxide was recorded on the Bruker IFS125HR Fourier transform spectrometer on the AILES Beamline at Synchrotron SOLEIL coupled to the newly developed corrosive gas multipass cell [20] set to a 10.88 m path length. The instrument was equipped with a Si/CaF_2 beamsplitter, InSb detector. The spectral resolution was chosen to give an apparatus function (0.0028 cm^{-1}) smaller than the Doppler width (ca. 0.0048 cm^{-1}) in the considered spectral domain. The spectrometer was evacuated to about 5×10^{-3} Pa in order to minimise H_2O and CO_2 absorptions. The instrument was operated with a 1.3 mm diameter entrance aperture and a quartz-halogen source, as the synchrotron source presents no advantage at this resolution in this spectral domain. The spectrum was ratioed against a single channel background spectrum of the empty cell which was recorded at a resolution of 0.04 cm^{-1} in order to ensure the best possible signal-to-noise in the ratioed spectrum. For the Fourier transform, a Mertz-phase correction with 2 cm^{-1} phase resolution, a zero-filling factor of 2 and no apodization (boxcar option) were applied to the averaged interferograms (896 scans). The spectrum was calibrated with residual CO_2 lines observed in the spectrum with their wavenumbers taken from HITRAN [13]. The standard deviation after calibration with well isolated CO_2 lines is 0.00005 cm^{-1} (one standard deviation). Thus, the estimated frequency accuracy of our measured lines is thus close to the CO_2 calibration lines reported accuracy (0.0001 cm^{-1}), perhaps 0.0002 cm^{-1}.

The NO_2 gas bottle used (Sigma-Aldrich, France 99.5%) was found to contain NO, N_2O and other impurities at a much higher level than the stated purity. It

was first purified following the standard procedure [3] by pumping on the frozen solid at about 200 K until the bluish colour due to the formation of N_2O_3 disappeared. This eliminated about 80% of the main impurities. We thus added a further step by letting 5 mmoles of the gas mixture react with about 0.5 mmole of ozone, prepared separately from 99.999% pure O_2. The remaining ozone and oxygen were removed by pumping above a cold bath at about 210 K. This successfully removed the NO and N_2O traces. The total pressure was measured using a Pfeiffer 10 hPa capacitive gauge. A small contamination due to CO_2 remained visible, but could be quantified to about 0.2% of the gas sample, using IR integrated intensity measurements and mass spectrometry. The MS measurements were collected from the same gas sample flask, with an instrument connected to the gas handling manifold. These were compared to a background spectrum of the instrument and collected within a few minutes to assess the CO_2 content'.

Q5

Assuming the contribution of foreign gases negligible, the total pressure (5.1 ± 0.1 hPa) can be attributed to the mixing of the monomer (NO_2) and dimer (N_2O_4) forms of nitrogen dioxide. These two forms exist in equilibrium, according to the equation ($2NO_2 \leftrightarrow N_2O_4$), with:

$$P^2(NO_2) = K_P P(N_2O_4) \quad (1)$$

where K_P is the equilibrium constant between NO_2 and N_2O_4, whose value depends on temperature [21] (at 296 K, $K_p = 123.3$ hPa) $P(NO_2)$ and $P(N_2O_4)$ are the partial pressures of the monomer and dimer, respectively. In such conditions, the monomer (NO_2) and dimer (N_2O_4) partial pressures can be estimated at about $P(NO_2) \approx 4.9 \pm 0.1$ hPa, $P(N_2O_4) \leq 0.2$ hPa.

3. Analysis

3.1. Overview of the analysis

A global view of the $2\nu_1$ and $\nu_1+\nu_3$ absorption bands (2627.3767 and 2906.074 cm^{-1}, respectively, for $^{14}N^{16}O_2$), is given on Figure 1. Also, detailed views of several spectral regions are presented in Figures 2–10. Because the $2\nu_1$ band is very weak relative to $\nu_1+\nu_3$ (see Table 1), the spectrum was recorded for a large (pressure × path length) product. In such conditions, the 2850–2930 cm^{-1} region, which corresponds to the $\nu_1+\nu_3$ band and its associated hot bands, is almost saturated. However, several windows of transparency exist which could be used to extend up to higher N and K_a values the analysis previously performed for $\nu_1+\nu_3$ by Mandin *et al.* [7].The analysis of the $2\nu_1$ band and the extension of the $\nu_1+\nu_3$ assignment was complicated for several reasons.

(i) These NO_2 bands are partially overlapped by the rather strong $\nu_1+\nu_{11}$ and $\nu_5+\nu_{11}$ bands of the N_2O_4 dimer located at 2631.5 and 2973.0 cm^{-1} [22], respectively.

(ii) Assignments in the far wings of the R-branch of $2\nu_1$ and the P-branch of $\nu_1+\nu_3$ bands are difficult because the lines are overlapped in the 2804–2850 cm^{-1} region, by transitions belonging to the hot bands associated to $\nu_1+\nu_3$.

According to the HITEMP predictions [17], the first hot bands associated to $\nu_1+\nu_3$ are in the following $R(\text{Hot}) = \text{Int}(\text{Hot\_band})/\text{Int}(\nu_1+\nu_3)$, intensity ratio at 296 K:

$$\begin{aligned} R(\nu_1+\nu_2+\nu_3-\nu_2) &= 0.025, \\ R(2\nu_1+\nu_3-\nu_1) &= 0.0032, \\ R(\nu_1+2\nu_3-\nu_3) &= 0.00077, \\ R(\nu_1+2\nu_2+\nu_3-2\nu_2) &= 0.00064. \end{aligned} \quad (2)$$

This means that, at 296 K, the $\nu_1+\nu_2+\nu_3-\nu_2$ and $2\nu_1+\nu_3-\nu_1$ hot bands are, respectively, ten times and twice as strong as $2\nu_1$. Although weaker, the contributions of the $\nu_1+2\nu_3-\nu_3$ and $\nu_1+2\nu_2+\nu_3-2\nu_2$ bands remain non-negligible as compared to $2\nu_1$.

To illustrate this point, Figure 2 gives a portion of the observed spectrum in the 2790–2830 cm^{-1} spectral region. The global structure of the computed 'HITEMP' spectrum ($2\nu_1$ band, $\nu_1+\nu_3$ band together with the associated hot bands) is in agreement with the observed spectrum. Unfortunately the HITEMP linelist proved to be not accurate enough for the identification of the interfering lines belonging to these hot bands. This is illustrated as an example on Figure 3 which gives the detailed view of this inter-comparison in the 2814.7–2815.5 cm^{-1} spectral region.

(iii) The prediction provided by the HITEMP database for the $2\nu_1$ band was not useful either. One of the reasons lies in the incorrect line intensity pattern provided for this band by HITEMP.

Figure 4 gives an overview of the present spectrum in the 2520–2790 cm^{-1} spectral range, together with the computed spectra generated for NO_2 using the $2\nu_1$ band linelists available in the HITEMP [17] and during the present work. For this inter-comparison, the HITEMP intensities were globally multiplied by a factor of ~2.8 in order to account for the fact that the $2\nu_1$ band intensity is underestimated by this factor in HITEMP. Figure 5 gives a detailed view of the P-branch in the 2537 cm^{-1} spectral region. It is clear that the observed $2\nu_1$ line intensity

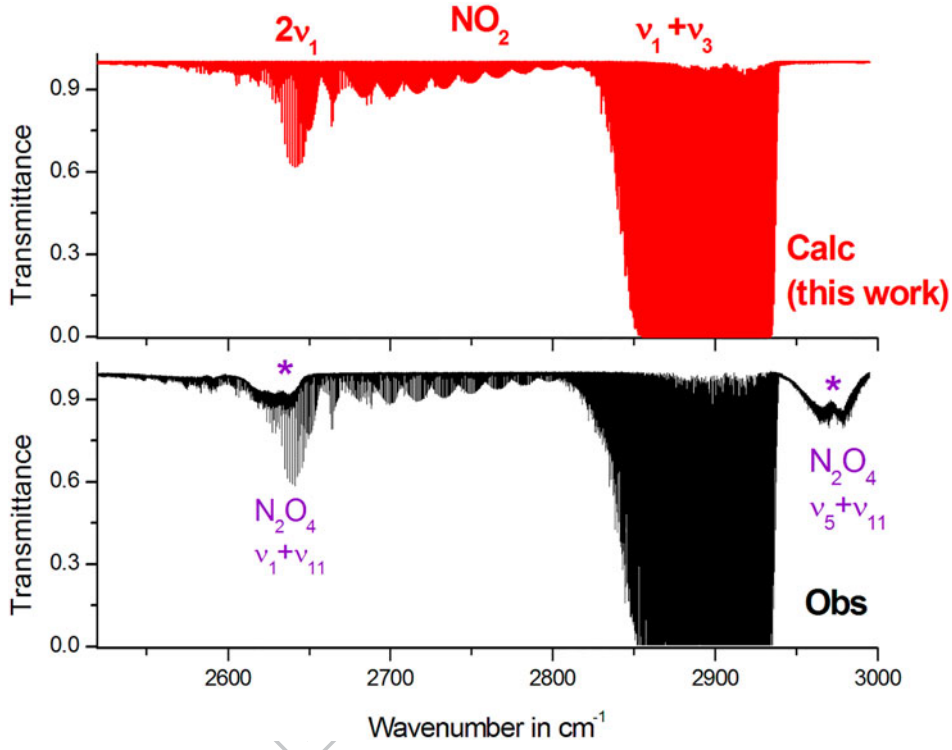

Figure 1. Overview of the $2\nu_1$ and $\nu_1 + \nu_3$ bands. The observed spectrum is compared to the present calculation.

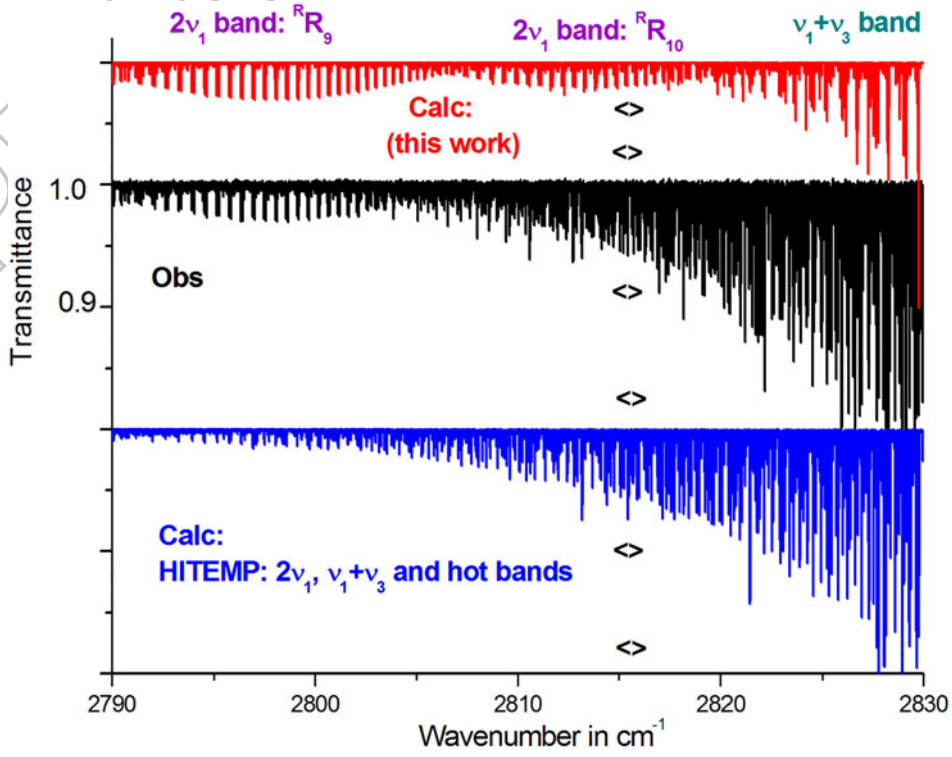

Figure 2. Detailed view and comparison of the predicted and observed NO_2 2790–2830 cm^{-1} $^RR_9$ and $^RR_{10}$ $2\nu_1$ and onset of $\nu_1+\nu_3$ P branches. For clarity, the calculated plots are shifted above (this work) and bellow (HITEMP) the observed line. The arrows region (< >) is viewed in more detail in the following figure.

Colour online, B/W in print

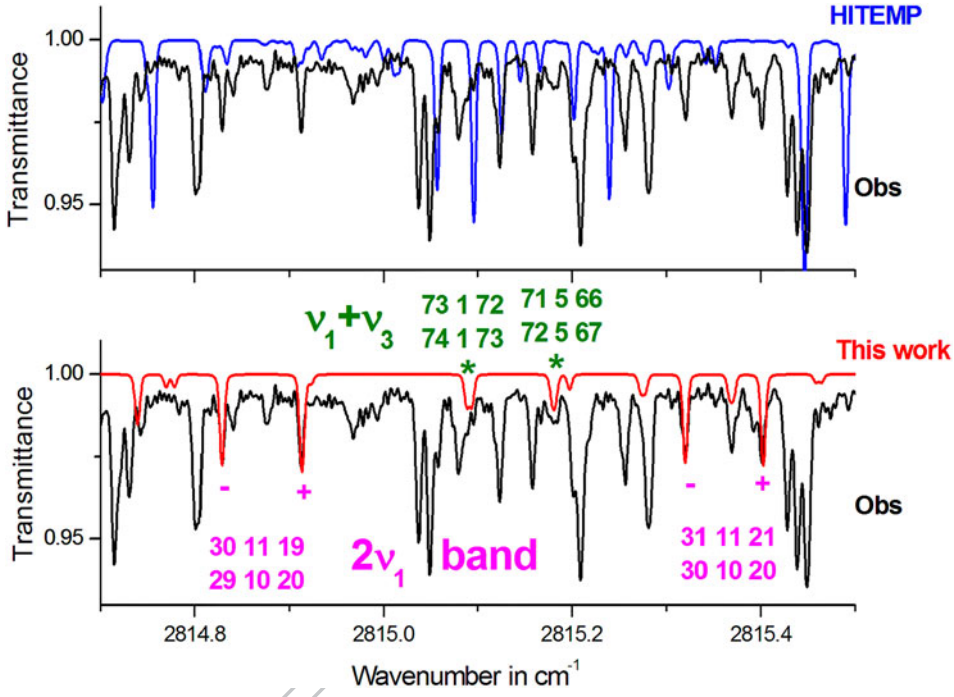

Figure 3. Detailed view of the 2815 cm^{-1} spectral region. The upper and lower traces compare the observed spectrum to line by line models performed using the HITEMP linelist (all bands) and the present calculation ($2\nu_1$ and $\nu_1+\nu_3$ bands), respectively. On the lower trace, some assignments are given for lines belonging to the $2\nu_1$ and $\nu_1+\nu_3$ bands and involving high N or K_a values.

Colour online, B/W in print

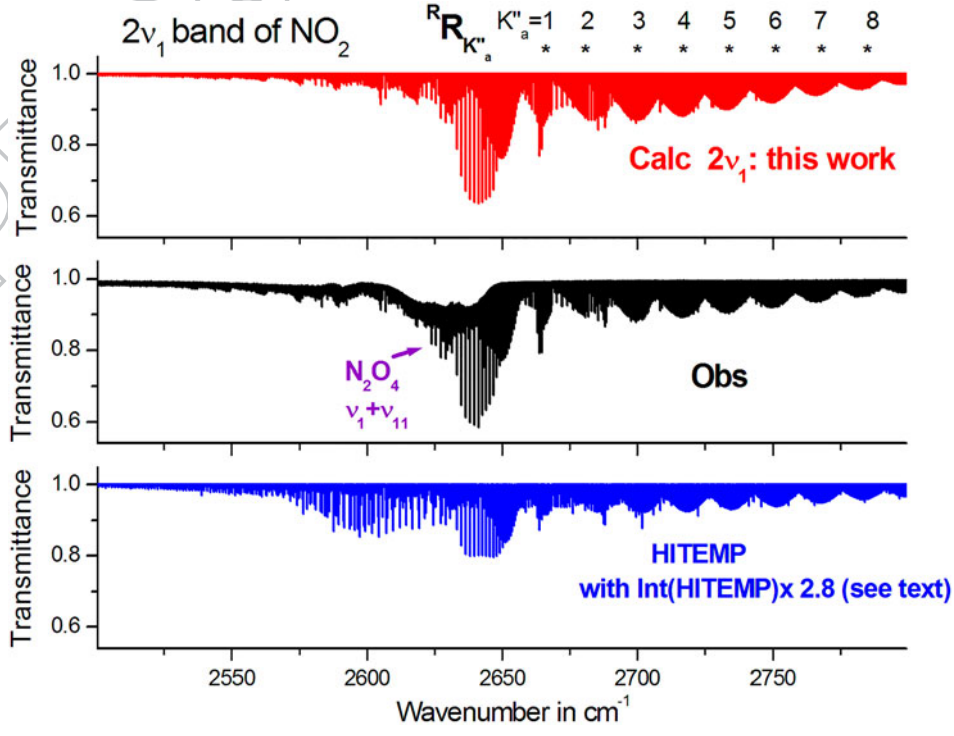

Figure 4. Overview of the $2\nu_1$ band in the 2500–2800 cm^{-1} spectral region. The observed spectrum (medium trace) is compared to line by line models of the $2\nu_1$ band performed using the HITEMP database [HITEMP] (bottom trace) and the linelist generated during this work (upper trace). For an easier inter-comparison, all HITEMP line intensities were multiplied, arbitrarily, by the band intensity ratio ($R = ({}^{\text{ThisWork}}\text{Int}(2\nu_1)/{}^{\text{HITEMP}}\text{Int}(2\nu_1)) \sim 2.8$) of the $2\nu_1$ band in these two linelists. Clearly the intensity pattern of the $2\nu_1$ band, with a very weak P-branch, also differs from the typical B-type scheme described by HITEMP. Note the absorption at 2631.5 cm^{-1} due to the $\nu_1+\nu_{11}$ band of N_2O_4 [22].

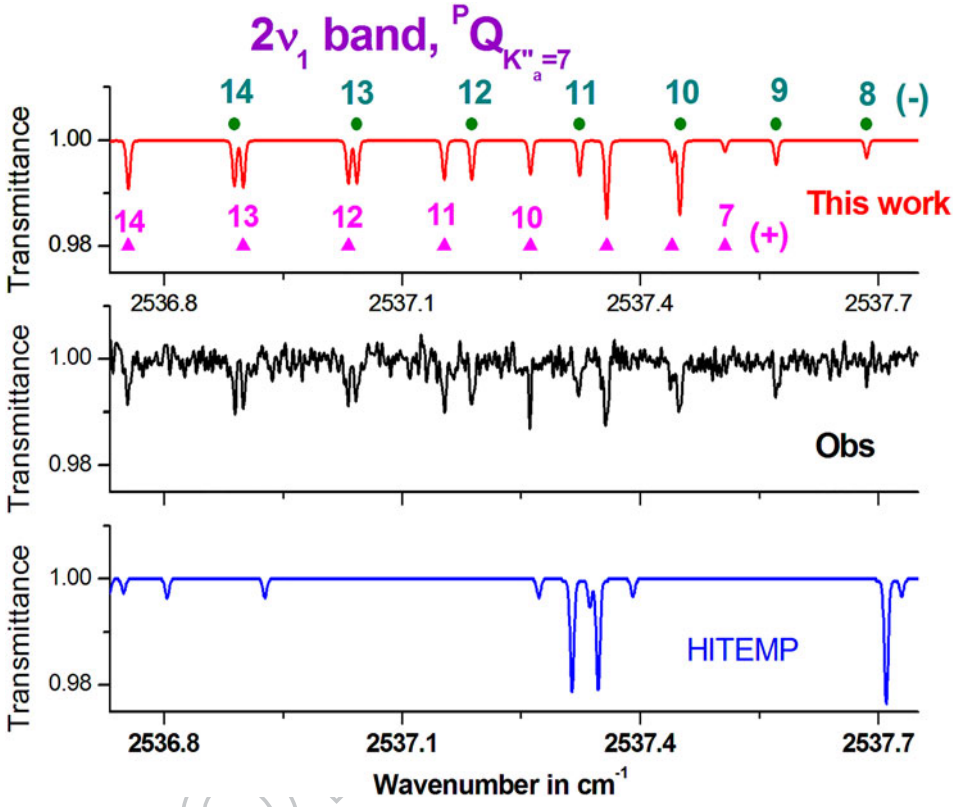

Figure 5. Portion of the observed spectrum in the 2536.8–2537.7 cm^{-1} spectral region. Lines from the ^{P}Q-branch of the $2\nu_1$ band are identified by the *N* value for the (+) and (−) spin-rotation components. The comparisons with the HITEMP and present linelists are also given.

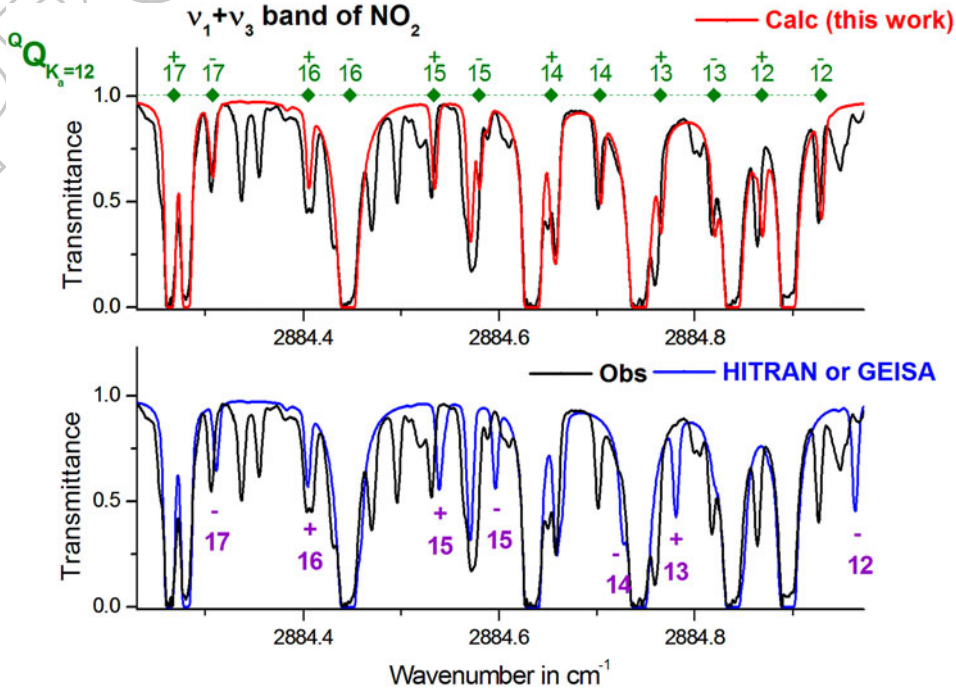

Figure 6. Portion of the NO_2 spectrum in the 2884 cm^{-1} region. The assignment for the $^{Q}Q_{12}$ subband of the $\nu_1 + \nu_3$ band is given. A comparison between the observed and calculated spectra is given, showing the progress achieved by the new $\nu_1 + \nu_3$ linelist as compared to the old one (HITRAN, GEISA).

Colour online, B/W in print

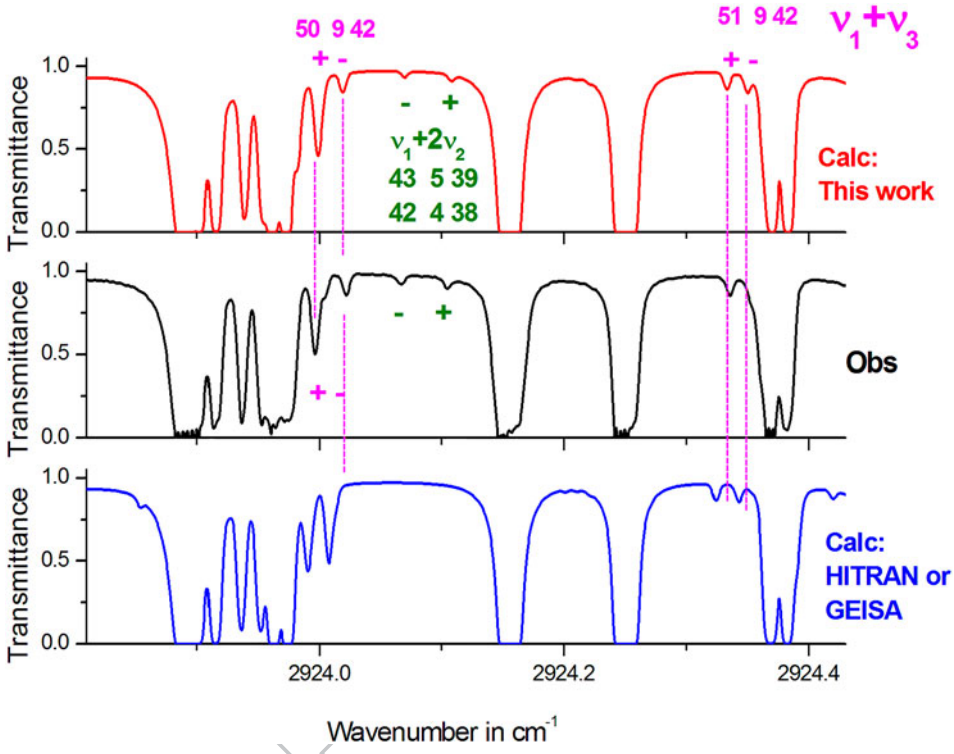

Figure 7. Portion of the NO_2 spectrum in the 2924 cm^{-1} region. Several lines belonging to the $\nu_1 + 2\nu_2$ dark band are observed for the first time. A comparison between the observed and calculated spectra is given, showing the progress achieved for the new $\nu_1 + \nu_3$ linelist as compared to the old one (HITRAN, GEISA). For the $\nu_1 + \nu_3$ band, the quoted assignments are the $[N, K_a, K_c]$ rotational quantum numbers in the (1,0,1) upper state, with '+' and '−' for $J = N + 1/2$ and $J = N - 1/2$, respectively.

Colour online, B/W in print

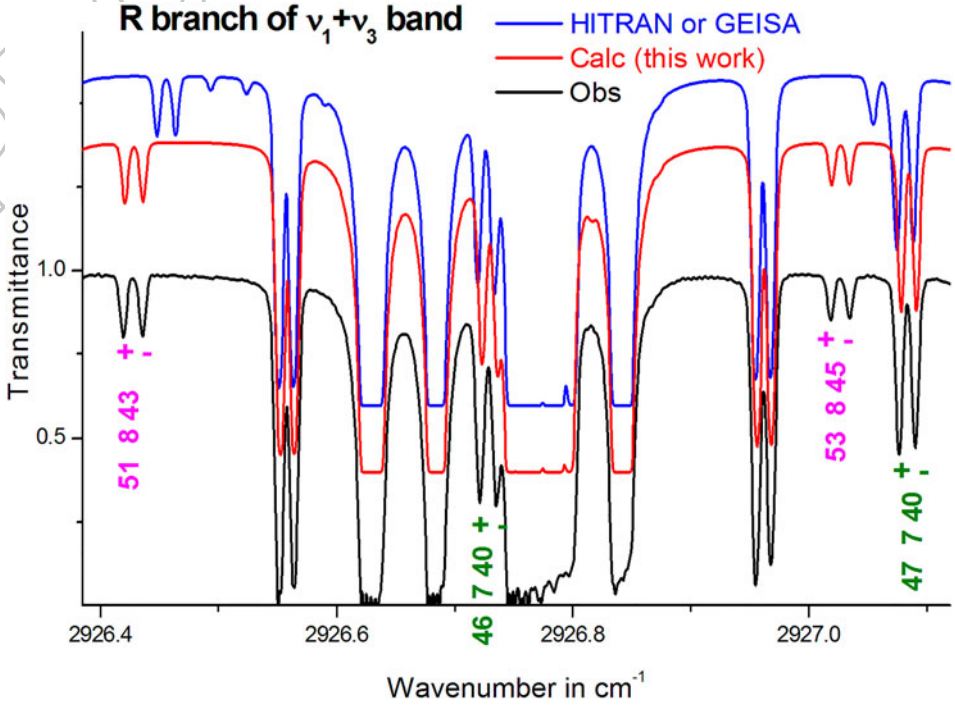

Figure 8. Portion of the NO_2 spectrum in the 2926 cm^{-1} region corresponding to the R-branch of the $\nu_1 + \nu_3$ band. The quoted assignments indicate that the $K_a = 8$ transitions are perturbed, and the comparisons between the observed and calculated spectra show the progress achieved for the new $\nu_1 + \nu_3$ linelist as compared to HITRAN-GEISA linelist. For the $\nu_1 + \nu_3$ band, the quoted assignments are the $[N, K_a, K_c]$ rotational quantum numbers in the (1,0,1) upper state, with '+' and '−' for $J = N + 1/2$ and $J = N - 1/2$, respectively. For clarity, the calculated plots are shifted above the observed line.

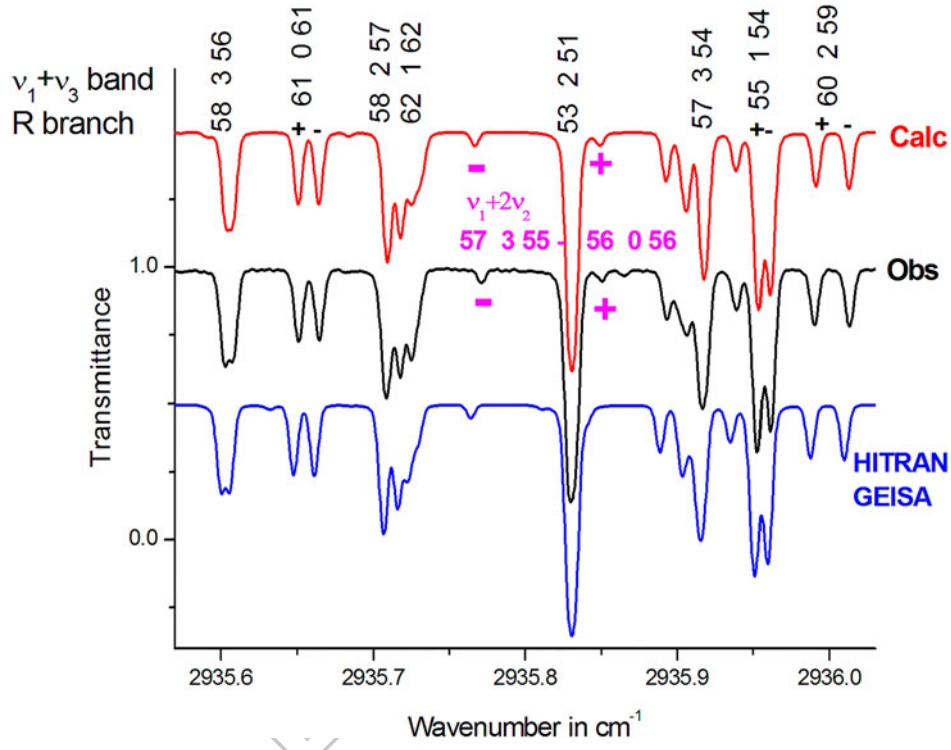

Colour online, B/W in print

Figure 9. Portion of the NO_2 spectrum in the 2935 cm^{-1} region. For the $\nu_1 + \nu_3$ band, the quoted assignments are the [N, K_a, K_c] rotational quantum numbers in the (1,0,1) upper state, with '+' and '−' for $J = N + 1/2$ and $J = N - 1/2$, respectively. The forbidden $\nu_1 + 2\nu_2$ [57,3,55]–[56,0,56] doublet lines is observed for the first time, because of a local resonance coupling together the (1,0,1) [$N = 57, K_a = 0, K_c = 57$] and (1,2,0) [$57, K_a = 3, K_c = 55$] resonating energy levels. A comparison between the observed and the calculated spectra using the present computation and the HITRAN-GEISA linelist is also given. For clarity, the calculated plots are shifted above and below the observed line.

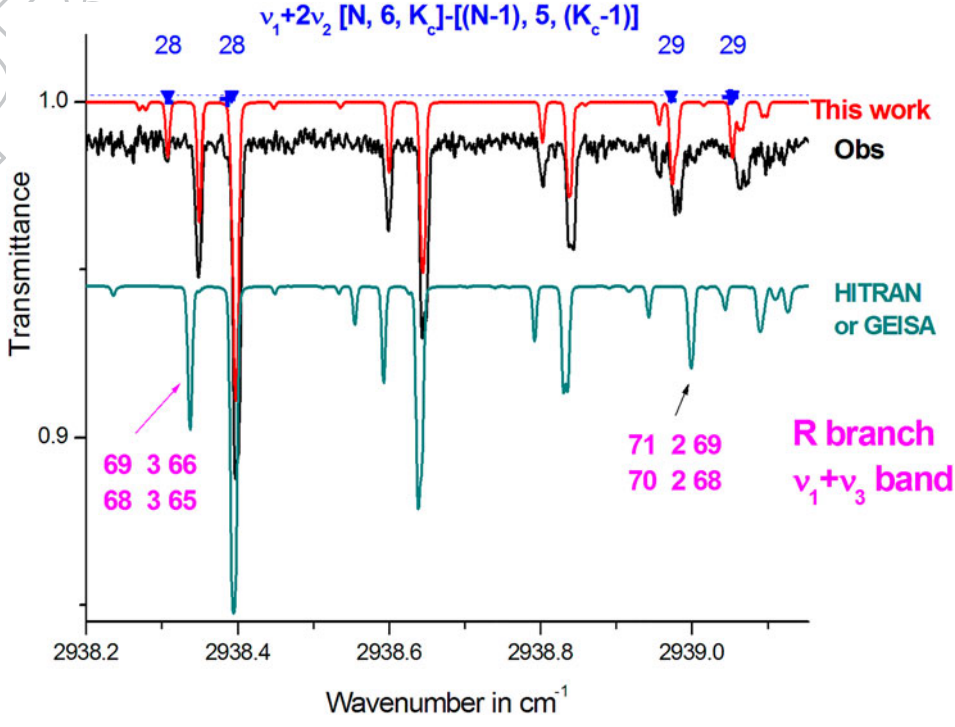

Colour online, B/W in print

Figure 10. Portion of the NO_2 spectrum in the 2938.6 cm^{-1} region. Several doublet lines belonging to the $\nu_1 + 2\nu_2$ dark band, involving $K'_a = 6, K''_a = 5$ in the (1,2,0) upper state, are observed for the first time. A comparison between the observed and calculated spectra (present work and the HITRAN-GEISA linelists) is given. For clarity, the calculated plots are shifted above and below the observed line.

pattern, with a very weak P-branch, differs significantly from the HITEMP prediction which corresponds to the 'classical' scheme for a B-type band.

3.2. Generation of the predicting linelist and assignments

The analysis of the $2\nu_1$ band and the updated assignments of the $\nu_1+\nu_3$ band were initiated by using predicting line lists (positions and intensities). For symmetry reasons, the $2\nu_1$ and $\nu_1+\nu_3$ bands of nitrogen dioxide are B-type and A-type bands, respectively, with (ΔK_a = odd and ΔK_c = odd), and (ΔK_a = even and ΔK_c = odd) selection rules, respectively. For this molecule, only $\Delta K_a = 1$ and $\Delta K_a = 0$ transitions are usually observable for B-type and A-type bands. Due to the spin-rotation interaction, each $^{14}N^{16}O_2$ transition is split in two sub components, which are most of the time easily observable in this spectral region.

The theoretical model used during this work accounts explicitly for both the spin-rotation resonances and for various vibration–rotational resonances and, as detailed in the next paragraph, this model was improved gradually during the assignment process. During the whole study, the ground state energy levels were calculated using the (0,0,0) ground state parameters of Ref. [23]. Finally the line intensities were computed using a method which will be presented further in the text.

As far as the $2\nu_1$ band is concerned, the first set of computed (2,0,0) energy levels were generated using, for the (2,0,0) upper state, the parameters (band centres, rotational, spin-rotation) generated in Ref. [10]. This predicted linelist helped us to perform the first assignments.

In parallel, the assignment of $\nu_1+\nu_3$ lines involving high N and K_a values was also performed using the same method. These weaker lines were observed in the far wing of the R-branch of $\nu_1+\nu_3$ or in several rather clear windows of transparency in the 3.44 µm region within very strong lines belonging either to the $\nu_1+\nu_3$ band or to various hot bands. In a similar way and for the first time, several lines could be identified for the dark $\nu_1+2\nu_2$ band: these very weak transitions could be observed in case of local resonances involving the (1,0,1) and (1,2,0) interacting states. These weak transitions are quite observable on Figures 7, 9, and 10. At a starting point of the identification process of these $\nu_1+\nu_3$ and $\nu_1+2\nu_2$ transitions, we used the parameters generated in Ref. [7] for the computation of the {(1,2,0), (1,0,1)} upper levels.

The calculated ground state energy levels were added to the observed line positions assigned during this work and during our previous investigations of the $\nu_1+\nu_3$ band [7] to get a preliminary set of experimental upper state spin-rotational energy levels for the (2,0,0), (1,0,1) and (1,2,0) states. These upper state levels were then introduced in a least squares fit to get refined values for the upper states parameters, therefore perform next new assignments, and then improve the model and the accuracy of the parameters, allowing then further new assignments. As it will be discussed later in the text, the final resonating scheme involves six resonating states {(2,0,0), (1,2,0), (1,0,1), (0,4,0), (0,2,1), (0,0,2)}, and we included in our list of experimental data the (1,0,1), (0,4,0), and (0,2,1) energy levels measured during the investigation of the $4\nu_2$, $2\nu_2+\nu_3$, and $2\nu_3$ bands [5].

These iterative processes were carried out until it was no more possible to perform further assignments. Table 2 describes the results of the present analyses which represent a very significant progress as compared to what could be done for the $2\nu_1$ ($N \leq 56, K_a \leq 10$) and $\nu_1+\nu_3$ ($N \leq 55$, $K_a \leq 10$) bands in Refs. [10] and [7], respectively. The list of observed line positions is given in supplementary data.

4. Theoretical model for the energy level computation

4.1. Description of the model

In this work, the v-diagonal operators are the sum of the Watson's type rotational operator [24] and of an electronic spin-rotational interaction operator [25]. Both operators are written for an A-type reduction and in an I^r representation. The $(v_1, v_2, v_3) \Longleftrightarrow (v'_1, v'_2, v'_3)$ v_i-off-diagonal operators are Fermi-type or C-type Coriolis operators, for $|\Delta v_3|$ = even and $|\Delta v_3|$ = odd, respectively.

In the very first step of the assignment process, the $2\nu_1$ band was considered as an isolated band. However, it was clear that the transitions involving high K_a values ($K_a \geq 8$) in the upper levels could not be satisfactorily reproduced. The very first identified resonance is a weak $|\Delta K_a| = 2$ Fermi resonance which involves the $K_a = 8$ energy levels of (2,0,0) with those in $K'_a = 6$ of (1,2,0). Starting for $K_a \geq 9$, the (2,0,0) levels are also involved in an additional C-type Coriolis resonance which couples levels in K_a of (2,0,0) to those in $K'_a = K_a - 1$ of (1,0,1). This is observed on Figure 6: indeed the transitions involving $K_a = 12$ in the (1,0,1) state are not predicted correctly by the HITRAN–GEISA linelist. Finally, when pursuing the investigation of the $\nu_1+\nu_3$ band, it appeared that, starting from $N = 65$, the (1,0,1) energy levels involving $K_a = 8$ are perturbed through a C-type Coriolis resonance with those in $K'_a = 5$ values of the (0,0,2) state. This is clearly observable in Figure 8 which shows that the $K_a = 8$ lines are shifted relative to their

Table 3. Hamiltonian matrix for the {(2,0,0), (1,2,0), (1,0,1), (0,4,0), (0,2,1), (0,0,2)} interacting vibrational states of $^{14}N^{16}O_2$.

	(2,0,0)	(1,2,0)	(1,0,1)	(0,4,0)	(0,2,1)	(0,0,2)
(2,0,0)	$W+SR$	F	C			
(1,2,0)	F	$W+SR$	C			
(1,0,1)	C	C	$W+SR$			C
(0,4,0)				$W+SR$	C	
(0,2,1)				C	$W+SR$	C
(0,0,2)			C		C	$W+SR$

Example of a Watson 'W' and spin-rotational 'SR' v-diagonal block:

		(v_1, v_2, v_3)	
		$N = J-1/2$	$N = J+1/2$
(v_1, v_2, v_3)	$N = J-1/2$	$W_{vv}+SR_{vv}$	SR_{vv}
	$N = J+1/2$	SR_{vv}	$W_{vv}+SR_{vv}$

Example of a Coriolis 'C' vibrational off-diagonal block (same form for a 'F' Fermi term):

		(v_1, v_2, v_3)	
		$N = J-1/2$	$N = J+1/2$
(v_1', v_2', v_3')	$N = J-1/2$	$C_{v'v}$ (resp. $F_{v'v}$)	
	$N = J+1/2$		$C_{v'v}$ (resp. $F_{v'v}$)

Notes: W_{vv}: Watson's A-type I^r representation Hamiltonian.

$$W_{vv} = E_v + [A^v - 1/2(B^v + C^v)]N_z^2 + 1/2(B^v + C^v)\mathbf{N}^2 + 1/2(B^v - C^v)N_{xy}^2 - \Delta_K^v N_z^4 - \Delta\Delta_{JK}^v N_z^2\mathbf{N}^2 - \Delta\Delta_J^v(\mathbf{N}^2)^2 - \delta\delta_K^v\{N_z^2, N_{xy}^2\} - 2\delta_J^v N_{xy}^2\mathbf{N}^2$$
$$+ H_K^v N_z^6 + H_{KJ}^v N_z^4\mathbf{N}^2 + H_{JK}^v N_z^2(\mathbf{N}^2)^2 + H_J^v(\mathbf{N}^2)^3 + h_K^v\{N_z^4, N_{xy}^2\} + h_{KJ}^v\{N_z^2, N_{xy}^2\}\mathbf{N}^2 + 2h_J^v N_{xy}^2(\mathbf{N}^2)^2 + \ldots$$

SR_{vv}: Electron spin-rotation interactions.

$$SR_{vv} = \varepsilon_{aa}^v S_a N_a + \varepsilon_{bb}^v S_b N_b + \varepsilon_{cc}^v S_c N_c + \Delta_N^{vS}(\mathbf{N}\cdot\mathbf{S}) + \frac{1}{2}\Delta_{NK}^{vS}\{\mathbf{N}^2 N_z S_z + S_z N_z \mathbf{N}^2\} + \Delta_{KN}^{vS} N_z^2(\mathbf{N}\cdot\mathbf{S}) + \Delta_K^{vS} N_z^3 S_z + \delta_N^{vS}(N_+^2 + N_-^2)(\mathbf{N}\cdot\mathbf{S})$$
$$+ \frac{1}{2}\delta_K^{vS}\{(N_+^2 + N_-^2)N_z S_z + N_z S_z(N_+^2 + N_-^2)\}$$

$C_{vv'}$: Coriolis-type interactions (for $|\Delta v_3| = $ odd).
$C_{vv'} = h_{vv'}^{1C} iN_y + h_{vv'}^{2C}\{iN_y, N_z^2\} + h_{vv'}^{3C} iN_y\mathbf{N}^2 + h_{vv'}^{4C}\{N_x, N_z\} + h_{vv'}^{5C}\{N_z^2, \{N_x, N_z\}\} + h_{vv'}^{7C}(N_-^3 - N_+^3) + \ldots H_{vv'}^{Anh}$: Anharmonic interactions, Fermi or Darling –Dennison, with $Anh = F$ and $Anh = DD$, respectively, with for a Fermi resonance.
$F_{vv'} = h_{vv'}^{0F} + h_{vv'}^{1F}\mathbf{N}^2 + h_{vv'}^{2F}N_z^2 + h_{vv'}^{4F}(N_x^2 - N_y^2)$ with: $N_{xy}^2 = N_x^2 - N_y^2$, $N_\pm = N_x \mp iN_y$, and $\{X, Y\} = XY + YX$.

computed positions in HITRAN or GEISA, while this is not the case for $K_a = 7$.

Including the (0,0,2) state in the resonating scheme has for consequence that six interacting states, {(2,0,0), (1,2,0), (1,0,1), (0,4,0), (0,2,1), (0,0,2)} have to be considered altogether during the final computation of energy levels. Let us remind that the (0,4,0) $\Longleftrightarrow$ (0,2,1) and (0,2,1) $\Longleftrightarrow$ (0,0,2) spin-rotation energy levels are also coupled by C-type Coriolis though (v_1, v_2, v_3) and (v_1, $v_2 \pm 2$, $v_3^- + 1$) 2d order resonances [5]. Table 3 describes this Hamiltonian matrix, together with the expansions of the various types of operators (rotational, spin-rotation, C-type Coriolis and Fermi) which are considered for the present computations. For consistency with the notations used in Ref. [18], the {(2,0,0), (1,2,0), (1,0,1), (0,4,0), (0,2,1), (0,0,2)} hexad of vibrational states will be labelled as the 'P4' block of resonating states in the rest of the text.

4.2. Least squares fit computation

A large set of experimental spin-rotational energy levels was introduced in a least squares fit calculation in order to get the parameters (vibrational energies, rotational, spin-rotation and interacting parameters) for the {(2,0,0), (1,2,0), (1,0,1), (0,4,0), (0,2,1), (0,0,2)} interacting states of $^{14}N^{16}O_2$. These data, which were obtained through analyses of Fourier transform spectra are of similar accuracy (positions at $\sim$ 0.0003–0.002 cm^{-1}, depending on the quality of the corresponding assigned lines) originate from the following sources:

- the set of (2,0,0), (1,0,1) and (1,2,0) experimental spin-rotational energy levels obtained during this work,
- the experimental energy levels obtained previously for the (1,0,1) [7] and the (0,4,0), (0,2,1), and (0,0,2) vibrational states [5].

During this fit, the vibrational energy of the (1,2,0) and (0,4,0) were fixed to the values obtained in a laser fluorescence study at $E_{120} = 2805.60\,\text{cm}^{-1}$ and $E_{040} = 2993.00\,\text{cm}^{-1}$ [26]. This is because there exists only a few identified energy levels for the (1,2,0) and (0,4,0) dark states. The resulting parameters for the {(2,0,0), (1,2,0), (1,0,1), (0,4,0), (0,2,1), (0,0,2)}

Table 4. Vibrational energies, rotational, spin-rotational, and Coriolis coupling constants for the {(2,0,0), (1,2,0), (1,0,1), (0,4,0), (0,2,1), (0,0,2)} interacting vibrational states of NO_2.

(A) Vibrational energies, spin-rotational and rotational constants

	(000)[a]	(2,0,0)	(1,2,0)	(1,0,1)	(0,4,0)	(0,2,1)	(0,0,2)
E_v		2627.37672(9)	2805.6 [b]	2906.07033(8)	2993.00 [b]	3092.47611(25)	3201.44828 (8)
A	8.00235469	8.1850348(109)	8.867339(210)	7.85295412(790)	9.60006(240)	8.5090199(660)	7.5540049(500)
B	0.433706798	0.429042117(485)	0.4337470(650)	0.428659206(200)	0.432505(220)	0.43077933(120)	0.428212425(630)
C	0.410442540	0.405272266(433)	0.4037196(670)	0.40502058(210)	0.408038(230)	0.40588662(120)	0.40520859(120)
Δ_K	$0.26878757 \times 10^{-2}$	$2.92843(140) \times 10^{-2}$	$0.398789(530) \times 10^{-2}$	$0.2678655(190) \times 10^{-2}$	$0.32018(980) \times 10^{-2}$	$0.408472(560) \times 10^{-2}$	$0.23808(190) \times 10^{-2}$
Δ_{KN}	-0.196822×10^{-4}	$-0.1576799(770) \times 10^{-4}$	$-0.204846(610) \times 10^{-4}$	$-0.226061(670) \times 10^{-4}$	#	$-0.272839(220) \times 10^{-4}$	$-0.24587(210) \times 10^{-4}$
Δ_N	0.2992447×10^{-6}	$0.297184(100) \times 10^{-6}$	$0.233255(410) \times 10^{-6}$	$0.308902(240) \times 10^{-6}$	$0.25899(380) \times 10^{-6}$	$0.306016(310) \times 10^{-6}$	$0.30663(220) \times 10^{-6}$
δ_K	0.40547×10^{-5}	$0.7261(130) \times 10^{-5}$	$-0.547465(590) \times 10^{-4}$	$1.08807(240) \times 10^{-5}$	#	$0.8266(300) \times 10^{-5}$	$-0.2326(210) \times 10^{-5}$
δ_N	0.3192774×10^{-7}	$0.315699(650) \times 10^{-7}$	$0.25111(580) \times 10^{-6}$	$0.310200\ (260) \times 10^{-7}$	#	$0.33671(280) \times 10^{-6}$	$0.35783(160) \times 10^{-7}$
H_K	0.303157×10^{-5}	$0.367967(170) \times 10^{-5}$	#	$0.309402(180) \times 10^{-5}$	#	$0.6514(130) \times 10^{-5}$	$0.26061(200) \times 10^{-5}$
H_{KN}	-0.270439×10^{-7}	$-0.538096(760) \times 10^{-7}$	#	$-0.11933\ (180) \times 10^{-7}$	#	#	0.0[c]
H_{NK}	0.2995×10^{-10}	#	#	$0.17658(180) \times 10^{-9}$	#	#	#
H_N	0.2866×10^{-12}	#	#	#	#	#	#
h_K	0.29297×10^{-7}	$0.6407(110) \times 10^{-7}$	#	$0.8043(200) \times 10^{-7}$	#	#	#
h_{KN}	-0.3637×10^{-10}	#	#	$-1.526(110) \times 10^{-10}$	#	#	#
h_N	0.1057×10^{-12}	#	#	#	#	#	#
L_K	-0.51104×10^{-8}	$-0.640448(110) \times 10^{-8}$	#	$-0.525422(520) \times 10^{-8}$	#	#	#
L_{KKN}	0.35117×10^{-10}	#	#	$-0.29648(150) \times 10^{-10}$	#	#	#
$\varepsilon_{aa}{}^{v}$	0.180353006	0.1868189(780)	0.21832(110)	0.1744702(550)	0. 261583 (720)	0.207550(590)	0.164756(700)
$\varepsilon_{bb}{}^{v}$	0.257833×10^{-3}	$0.21513(840) \times 10^{-3}$	#	$0.29742(560) \times 10^{-3}$	#	#	#
$\varepsilon_{cc}{}^{v}$	$-0.3178107 \times 10^{-2}$	$-0.345718(710) \times 10^{-2}$	$-3.4552(330) \times 10^{-2}$	$-0.338023(56) \times 10^{-2}$	$-0.34810(710) \times 10^{-2}$	$-0.33524(120) \times 10^{-2}$	$-0.31528(130) \times 10^{-2}$
$\Delta_K{}^{vS}$	-0.17606×10^{-3}	$-0.202271(840) \times 10^{-3}$	#	$-0.173272(450) \times 10^{-3}$	#	$-0.2689(220) \times 10^{-3}$	$-0.1609(120) \times 10^{-3}$
$\Delta_{KN}{}^{vS} + \Delta_{NK}{}^{vS}$	0.6005×10^{-6}	#	#	$0.9344(240) \times 10^{-6}$			

Higher order spin-rotational and rotational constants for all states

Rotational constants[#]		Spin-rotational constants[#]	
H_N	0.2866×10^{-12}	Δ_N^{vS}	0.6322×10^{-9}
h_N	0.1057×10^{-12}	Δ_{NK}^{vS}	0.1678×10^{-5}
L_{KN}	0.12158 × 10–12	H_K^S	0.29673 × 10–6
P_K	0.867×10–11	L_K^S	−0.3569 × 10–9

(*continued*)

Table 4. Continued.

Fermi resonances						
Operator	(2,0,0)–(1,2,0)					
$_{QK}$	−0.839×10−14					
(B) Off-diagonal in *v*-Fermi or Coriolis operators Coriolis resonances						
	$iN_y \times 10^1$	$\{N_x, N_z\} \times 10^2$	$iN_y N^2 \times 10^6$	$\{N_z^2, iN_y\} \times 10^3$	$\{N_z^2, \{N_x, N_z\}\} \times 10^4$	$(N_-^3 - N_+^3) \times 10^5$
(1,0,1)–(1,2,0)	−0.4684(210) (−0.301252 [7])	−0.36193(910)		+0.8619(350)		
(0,0,2)–(1,0,1)	0.166245(990)					0.367546(420)
(0,0,2)–(0,2,1)	−0.41154(152) (−0.39643 [5])					
(0,2,1)–(0,4,0)	−0.754912(520) (−0.754144 [5])		0.948(110) (0.7294 [5])			
(1,0,1)-(2,0,0)					0.58952(120)	0.23948(230)
Fermi resonances						
Operator	(2,0,0)–(1,2,0)					
N_z^2	−0.14771(110)					
$(N_x^2 - N_y^2)$	$-0.29527(480) \times 10^{-3}$					

Note: The results are in cm^{-1} and the quoted errors correspond to one standard deviation. The spin-rotational constants, the higher order rotational constants together with constants marked with # were held fixed to the ground state values [23]. For the off-diagonal Coriolis constants (in Part B), the values achieved during previous investigations [5,7] are also given.

[a]From Ref. [23].

[b]From Ref. [26].

[c]Fixed at zero (non-determinable).

Table 5. Statistical analysis on the energy level calculation.

	(2,0,0)	(1,2,0)	(1,0,1)	(0,4,0)	(0,2,1)	(0,0,2)
Number of spin-rotation levels:	993	38	1296	41	499	490
$0 \leq \delta \leq 0.001$	85.3%	34.2%	70.8%	26.8%	64.1%	74.9%
$0.001 \leq \delta \leq 0.002$	12.0%	23.7%	17.3%	34.2%	25.7%	17.8%
$0.002 \leq \delta \leq 0.006$	2.7%	42.1%	11.4%	39.0%	10.0%	7.3%
$0.006 \leq \delta \leq 0.009$			0.5%		0.2%	

Note: $\delta = |E_{obs} - E_{calc}|$ in cm^{-1}. Standard deviation: 0.92×10^{-3} cm^{-1}.

interacting states of $^{14}N^{16}O_2$ are quoted together with their uncertainties in Table 4. Note that, for the ν_i-diagonal rotational or spin-rotational operators, the main and centrifugal distortion constants that could not be determined by the fit were held fixed at their values achieved for the ground state values [23]. Indeed this strategy differs from the one adopted in Ref. [5] where the constants which could not be determined were fixed at zero during the computation of the {(0,4,0), (0,2,1), (0,0,2)} interacting states of $^{14}N^{16}O_2$.

An important point is the problem of the sign of the parameters determined during this work. As usual, the absolute signs of all the parameters involved in the expansion of the ν_i-diagonal operators (Watson's type or spin-rotation) are determined during the least squares fit calculation. This is also the case for the *relative* signs of all the parameters involved in the expansion of any given Fermi- or Coriolis operators. On the other hand, the results of the present energy level calculation remain unchanged during any of these global changes of sign in these off-diagonal operators:

$$C_{040,021} \rightarrow -C_{040,021},$$
$$\text{or, } C_{101,002} \rightarrow -C_{101,002},$$
$$\text{or, } C_{021,002} \rightarrow -C_{021,002}. \quad (3)$$

Q6

However, the global signs of the $F_{200,120}$, $C_{120,101}$, and $C_{200,101}$ blocks are not fully determined or independent since the possible signs changes are

$$(F_{200,120} \rightarrow -F_{200,120} \textit{ and } C_{120,101} \rightarrow -C_{120,101}),$$
$$\text{or } (F_{200,120} \rightarrow -F_{200,120} \textit{ and } C_{200,101} \rightarrow -C_{200,101}),$$
$$\text{or } (C_{120,101} \rightarrow -C_{120,101} \textit{ and } C_{200,101} \rightarrow -C_{200,101}). \quad (4)$$

The results of the computation proved to be satisfactory according to the statistical analysis which is provided in Table 5. The results of this calculation are given in as a supplementary data.

4.3. Wavefunctions and percentage of mixing

The wavefunctions issued from the diagonalization of the Hamiltonian matrix are written in the following way for a given $|N, K_a, K_c, S, J>$ energy level of the $V = (\nu_1,\nu_2,\nu_3) = (2,0,0), (1,2,0), (1,0,1), (0,4,0), (0,2,1),$ or (0,0,2) vibrational state:

$$|V'; N'K'_aK'_cSJ'\rangle = \sum_{\nu' \in P4} \sum_{N'_0,k',\gamma'} C^{V;N'K'_aK'_cJ'}_{\nu';N'_0k'\gamma'} |\nu'\rangle |N'_0k'SJ'\gamma'\rangle. \quad (5)$$

In this expression, $|N'_0k'SJ'\gamma'\rangle$ are the Wang's type symmetrised base functions for spin-rotation wavefunctions with $S = ½$. The summation holds for $N'_0 = J' + 1/2$ and $N'_0 = J' - 1/2$, with $\gamma'_i = \pm 1$ depending on the symmetry type of the considered energy level [3]. Also the ν'_i summation is made on P4 block, and $C^{V;JNK'_aK'_c}_{\nu';N'_0k'\gamma'}$ are the terms involved in the expansion of the upper state wavefunctions in the right-hand side of Equation (5).

A similar expression holds also for the ground vibrational state

$$|0; NK_aK_cSJ\rangle = \sum_{N_0,k,\gamma} C^{0;JNK_aK_c}_{0;N_0k\gamma} |0\rangle |N_0kSJ\gamma\rangle. \quad (6)$$

To characterise the vibration resonances, it is interesting to calculate the $\%(N', K'_a)^{V'}_{\nu'}$ mixing ratio of the $|V', N'K'_aK'_cSJ'\rangle$ wavefunction into the $\nu' = (\nu'_1, \nu'_2, \nu'_3)$ state, which is defined as

$$\%(N', K'_a)^{V'}_{\nu'} = \sum_{N'_0k'\gamma'} |C^{V';JN'K'_aK'_c}_{\nu';N'_0k'\gamma'}|^2. \quad (7)$$

4.4. Discussion

The theoretical model used here for the {(2,0,0), (1,2,0), (1,0,1), (0,4,0), (0,2,1), (0,0,2)} six interacting states is a 'local effective model' which tries to model as accurately as possible the experimental levels available for this set of interacting states, accounting explicitly for the resonances each time there were observed.

This strategy differs from the one developed during the NO_2 'global model' computation [18]. During this computation, a block diagonalization of the NO_2 vibrational states was performed. The ν_1-type, ν_2-type, and ν_3-type vibrational expansion of the rotational, spin-rotational and interacting constants involved in the description of the block Hamiltonian matrices were determined through a least squares fit calculation performed on the whole set of experimental line positions collected in the literature for NO_2 in the 0.006–7916 cm^{-1} spectral range. However, it is clear that the set of experimental energy levels available at that time [18] for the P4

vibrational states was less extended or less accurate than during the present study.

For the resonating states belonging to the set of {(2,0,0), (1,2,0), (1,0,1), (0,4,0), (0,2,1), (0,0,2)} interacting states, the type of resonances which are in principle observable depends on symmetry considerations.

4.5. The Fermi and Darling–Dennison resonances

For Δv_3 = even, Fermi (v_1, v_2, v_3) $\Longleftrightarrow$ ($v_1^- + 1$, $v_2 \pm 2$, v_3) or Darling–Dennison (v_1, v_2, v_3) $\Longleftrightarrow$ ($v_1^- + 2$, v_2, $v_3 \pm 2$) resonances are symmetry-allowed. In fact, only the Fermi resonance coupling the (2,0,0) $\Longleftrightarrow$ (1,2,0) states could be evidenced during this work. Indeed the $K_a = 8$ energy levels of the (2,0,0) state are in resonance with those in $K_a = 6$ levels of the (1,2,0) state, with a maximum mixing ratio of 49% for $N = 68$. In the expansion of the Fermi operator which is given in Table 4, only the rotational terms in $(N_x^2 - N_y^2)$ and $\{N_z^2, (N_x^2 - N_y^2)\}$ could be determined through this least squares fit calculation. As usual for a classical least squares fit calculation, we could not get any information on the zero order term $h_{vv'}^{0F}$.

On the other hand, the effects of other possibly-existing Fermi or Darling–Dennison resonances were not observed and were not accounted for explicitly. In Ref. [18] these resonances couple the spin-rotation levels of the (1,2,0) $\Longleftrightarrow$ (0,4,0) and (1,0,1) $\Longleftrightarrow$ (0,2,1) interacting states, for the Fermi resonances, and the (2,0,0) $\Longleftrightarrow$ (0,0,2) states for the Darling–Dennison resonances. We tried to introduce these resonances during our fit by fixing the parameters involved in the description of these resonances to the values predicted by this global model. However, in such conditions, the energy levels computation failed completely.

4.6. The Coriolis resonances

For Δv_3 = odd, the (v_1, v_2, v_3) $\Longleftrightarrow$ ($v_1^- + 1$, v_2, $v_3 \pm 1$) first-order and (v_1, v_2, v_3) $\Longleftrightarrow$ (v_1, $v_2^- + 2$, $v_3 \pm 1$) second-order C-Type Coriolis resonances are presumed to occur.

4.6.1. First-order C-type Coriolis resonances

During the present work the first order C-type Coriolis resonances coupling the (2,0,0) $\Longleftrightarrow$ (1,0,1) and (1,0,1) $\Longleftrightarrow$ (0,0,2) levels were accounted for. Indeed the (1,0,1) [N, K_a K_c, J] energy levels involving high K_a values ($K_a \geq 9$) are involved in strong resonances with the levels in $K'_a = K_a + 1$ of (2,0,0). To give an order of magnitude, the $\%(N, K_a)^{(1,0,1)}_{(2,0,0)}$ mixing ratio grows up to 4.4% for $N = 41$ and $K_a = 13$.

As far as the (1,0,1) $\Longleftrightarrow$ (0,0,2) interacting states are concerned, we had to account for the rather strong $|\Delta K_a| = 3$ local C-type Coriolis resonance which couples the $K_a = 8$ series of (1,0,1) with those in $K_a = 5$ of (0,0,2). However, for the range of observed energy levels concerned by this study, we did not observe any perturbation in $|\Delta K_a| = 1$ coupling these energy levels, and the first-order term (in iN_y) in the expansion of the Coriolis operator could not be determined.

4.6.2. Second-order C-type Coriolis resonances

As pointed out during our previous investigations of the $v_1 + v_3$ band [7], and of the $2v_3$, $2v_2 + v_3$, and $4v_2$ interacting bands [5], the (1,2,0) $\Longleftrightarrow$ (1,0,1), the (0,4,0) $\Longleftrightarrow$ (0,2,1) and (0,2,1) $\Longleftrightarrow$ (0,0,2) energy levels are coupled through C-type second-order Coriolis resonances. The comparisons between the previous and new values of the parameters involved in the expansion of the C-type Coriolis operators are given in Table 4.

For the (0,4,0), (0,2,1), and (0,0,2) interacting states, the expansion of the C-type Coriolis operator takes the same form as in our previous study, and the values of the first-order term the $h^{1C}_{(v_1,v_2,v_3)(v_1,v_2+2,v_3-1)}$ parameters do not differ significantly from the ones obtained during our previous investigation. This is expected because as compared to our previous investigation, no new experimental data are available for the (0,4,0), (0,2,1), and (0,0,2) interacting states.

On the other hand, the expansion of the (1,0,1) $\Longleftrightarrow$ (1,2,0) C-type Coriolis operator takes a form which is now significantly more complex (with terms in $\{N_x, N_z\}$ and in $\{iN_y, N_z^2\}$), and the value of the first-order term (in iN_y) is larger than in 1997 [7]. This is because the set of available experimental energy levels for the bright (1,0,1) and dark (1,2,0) states is now extended (see Table 2). Also, the resonating scheme involving these states is more complex that what was observed in 1997 [7]. In addition to the $|\Delta K_a| = 1$ C-type Coriolis resonances which couple the $K_a = 4$ and $K_a = 5$ of (1,0,1) to those in $K'_a = 5$ and $K'_a = 6$ of (1,2,0), respectively, a local $|\Delta K_a| = 3$ resonance involves the (1,0,1) [$N = 57$, $K_a = 0$, $K_c = 57$] and (1,2,0) [57, $K_a = 3$, $K_c = 55$] resonating energy levels. Let us remind that the (1,0,1) (resp. (1,2,0)) energy levels are also involved in Coriolis resonances with levels belonging to the (2,0,0) and (0,0,2) states (resp. in Fermi resonances with (2,0,0)).

To be complete, let us mention that we did not observe any noticeable spin-rotation resonance within the (1,0,1), (1,2,0) or (2,0 0) energy levels. This type of resonance, with ($\Delta J = 0$ and $\Delta N = \pm 2$) selection rules, was already observed within the (0,0,0) or (0,0,1) vibrational states [3].

5. Line intensities

As mentioned previously the line assignments for $2\nu_1$, $\nu_1+2\nu_2$ and $\nu_1+\nu_3$ were performed thanks to predictions on line positions and intensities performed for these bands.

As one can guess by reading the first part of this paper, getting accurate intensities for the $2\nu_1$ band is not an easy task.

As mentioned previously, the $2\nu_1$ band of NO_2 is masked partially by the strong $\nu_1+\nu_{11}$ band of the N_2O_4 dimer. In such conditions, even the high-quality cross-sections measured at the Pacific Northwest National Laboratory (PNNL) for NO_2 and N_2O_4 [27] can only provide a rough estimation ($\mathrm{Int}(2\nu_1)/\mathrm{Int}(\nu_1+\nu_3)\sim 1/350$) of the band intensity ratio of the $2\nu_1$ and $\nu_1+\nu_3$ bands. It is clear also that the PNNL data cannot provide information on the anomalous line intensity pattern of the $2\nu_1$ band.

During this work, we determined the expansion of the $2\nu_1$ transition moment operator through a least squares fit performed on individual $2\nu_1$ experimental line intensities. Owing to the difficulties which were already mentioned in this text (partial overlapping with an absorption due to N_2O_4, presence of a nearby very strong band) it is clear that these $2\nu_1$ line intensities, which were obtained using a single FTS spectrum, cannot be considered as very accurate.

5.1. Experimental intensities

Line intensities were retrieved from only one individual spectrum using a mono-spectrum non-linear least squares fitting program, already used and described in previous works [30,32]. Briefly, the measurements involved the adjustment of a calculated spectrum to the observed spectrum, using a non-linear least squares fitting procedure. Calculated spectrum was computed as the convolution of a Voigt-type transmission spectrum with an instrument line shape function, which included the effects of the finite maximum optical path difference and of the finite source aperture diameter of the interferometer [33]. In the present work, no deviation from this instrument line shape model was observed using the nominal aperture diameter of 1.3 mm. The measurements were carried out on small spectral intervals, ranging from 0.1 to 0.5 cm^{-1} and containing one to several lines. The background spectrum was represented by an affine function and the profile of the lines was modelled using a Voigt function with Gaussian width always held fixed to the value calculated for the Doppler broadening. For each line, the position, the $S*P$ (S is the integrated absorption coefficient per unit pressure, also known as the absolute intensity and P the pressure) product, the Lorentzian widths of the Voigt profile can be determined. The line intensities S (in cm^{-2}/atm) can be derived and a total of 93 individual line intensities were obtained.

Line intensities were retrieved from only one individual spectrum it is therefore difficult to make a realistic analysis of the uncertainties. We can only give a rough estimate of about 20% on the line intensities. The list of measured line intensities are quoted in Table 6.

5.2. Theory

A detailed description of the method which is used to compute the NO_2 line intensities was given in Refs. [3,7,34].

The intensity, $k_{\tilde{\nu}}^{N}(T)$, of a line of a pure $^{14}N^{16}O_2$ isotopic sample is given (in $\mathrm{cm}^{-1}/(\mathrm{molecule}\times\mathrm{cm}^{-2})$) by [3]:

$$k_{\tilde{\nu}}^{N}(T)=\frac{8\pi^3\tilde{\nu}}{4\pi\varepsilon_0 3hc}\exp\left(-\frac{E_L}{kT}\right)\times\left(1-\exp\left(-\frac{\tilde{\nu}}{kT}\right)\right)\frac{g_L}{Z(T)}R_L^U. \quad (8)$$

Note that for a 'natural sample' of NO_2, this expression is multiplied by $a=0.991616$ (Ref. [35]) to account for the $^{14}N^{16}O_2$ isotopic concentration in the 'natural' sample of nitrogen dioxide.

In this expression $\tilde{\nu}=(E_U-E_L)/hc$ is the wavenumber of the transition, and E_L and E_U are the energies of lower $L=|0;NK_aK_cSJ\rangle$ and upper $U=|V;N'K'_aK'_cSJ'\rangle$ levels of the transition (in cm^{-1}). Here we are dealing with cold bands, and the lower and upper states of the transition are the ground vibrational state $|0>=[(0,0,0)>$ and the $V'=(\nu'_1,\nu'_2,\nu'_3)$ state, respectively. In Equation (8), $4\pi\epsilon_0=1$, because we are using Debye unit for the dipole moment. The total partition function, $Z(T)=Z_{\mathrm{vib}}(T)\times Z_{\mathrm{rot}}(T)$, includes the nuclear spin contribution ($g_L=2I+1=3$ for $^{14}N^{16}O_2$), and we used for the total partition the value $Z(296\,\mathrm{K})=13{,}618$ which is in reasonable agreement with the value quoted in HITRAN [13]. Finally, R_L^U is the square of the matrix element of μ'_z:

$$R_L^U=\left|\langle V;N'K'_aK'_cSJ'|\mu'_z|0;NK_aK_cSJ\rangle\right|^2. \quad (9)$$

The expansion of the upper and lower state wavefunctions have been given in Equations (5) and (6). Also, μ'_z is the transformed dipole moment operator, which is expanded as

$$\mu'_z=\sum_{\nu'}|0\rangle\langle\nu'|^{0,\nu'}\mu'_z. \quad (10)$$

In this expression, ν' is one of the {(2,0,0), (1,2,0), (1,0,1), (0,4,0), (0,2,1), (0,0,2)} interacting states of $^{14}N^{16}O_2$.

Table 6. List of the observed and computed line intensities (in $cm^{-1}.atm^{-1}$) at 296 K for the $2\nu_1$ band of NO_2 (for a 'pure sample' of $^{14}N^{16}O_2$).

N′	K'_a	K'_c	J′	N″	K''_a	K''_c	J″	Sigma	Int_obs	Int_calc	O–C in %
13	2	12	+	13	3	11	+	2589.4270	7.51E−05	6.83E−05	9.1%
13	2	12	−	13	3	11	−	2589.4881	7.35E−05	6.31E−05	14.1%
11	2	10	+	11	3	9	+	2589.6839	7.18E−05	6.38E−05	11.1%
20	0	20	−	20	1	19	−	2615.0156	1.28E−04	1.23E−04	3.9%
18	0	18	+	18	1	17	+	2615.9169	1.39E−04	1.41E−04	−1.7%
19	1	19	+	18	2	16	+	2616.4364	1.05E−04	9.94E−05	5.3%
19	1	19	−	18	2	16	−	2616.4897	1.07E−04	9.46E−05	11.7%
16	0	16	+	16	1	15	+	2616.7397	1.82E−04	1.50E−04	17.9%
16	0	16	−	16	1	15	−	2616.7685	1.65E−04	1.41E−04	14.6%
17	1	17	+	16	0	16	+	2646.2815	4.79E−04	4.58E−04	4.4%
19	1	19	+	18	0	18	+	2647.2331	5.41E−04	5.09E−04	5.9%
21	1	21	+	20	0	20	+	2648.1239	5.78E−04	5.47E−04	5.3%
23	1	23	+	22	0	22	+	2648.9594	5.99E−04	5.72E−04	4.6%
25	1	25	+	24	0	24	+	2649.7452	6.09E−04	5.80E−04	4.7%
25	1	25	−	24	0	24	−	2649.7616	5.78E−04	5.57E−04	3.7%
31	1	31	+	30	0	30	+	2651.8590	5.48E−04	5.18E−04	5.4%
31	1	31	−	30	0	30	−	2651.8781	5.35E−04	5.01E−04	6.3%
35	1	35	+	34	0	34	+	2653.1129	4.45E−04	4.24E−04	4.6%
35	1	35	−	34	0	34	−	2653.1329	4.19E−04	4.12E−04	1.8%
46	0	46	+	45	1	45	+	2653.2733	1.83E−04	1.47E−04	19.8%
37	1	37	+	36	0	36	+	2653.7042	4.04E−04	3.71E−04	8.2%
37	1	37	−	36	0	36	−	2653.7246	3.87E−04	3.61E−04	6.7%
39	1	39	+	38	0	38	+	2654.2746	3.40E−04	3.17E−04	6.8%
39	1	39	−	38	0	38	−	2654.2955	3.19E−04	3.08E−04	3.4%
41	1	41	+	40	0	40	+	2654.8256	2.82E−04	2.65E−04	6.1%
41	1	41	−	40	0	40	−	2654.8478	2.64E−04	2.57E−04	2.6%
45	1	45	−	44	0	44	−	2655.8873	1.86E−04	1.69E−04	9.2%
47	1	47	+	46	0	46	+	2656.3630	1.37E−04	1.36E−04	1.2%
11	2	10	+	10	1	9	+	2658.8395	1.49E−04	1.52E−04	−1.8%
16	2	14	−	15	1	15	−	2664.5391	1.81E−04	1.89E−04	−4.7%
16	2	14	+	15	1	15	+	2664.5813	1.74E−04	2.01E−04	−15.4%
39	2	38	−	38	1	37	−	2668.0291	1.60E−04	1.52E−04	4.7%
24	2	22	+	23	1	23	+	2672.1788	2.19E−04	2.08E−04	4.8%
26	2	24	−	25	1	25	−	2674.1783	1.72E−04	1.86E−04	−8.2%
26	2	24	+	25	1	25	+	2674.2250	1.81E−04	1.93E−04	−6.5%
10	3	7	+	9	2	8	+	2674.7134	1.34E−04	1.40E−04	−4.6%
11	3	9	+	10	2	8	+	2675.4237	1.53E−04	1.57E−04	−3.0%
28	2	26	−	27	1	27	−	2676.2952	1.51E−04	1.67E−04	−10.1%
13	3	11	−	12	2	10	−	2676.7905	1.75E−04	1.77E−04	−1.2%
13	3	11	+	12	2	10	+	2676.8454	1.95E−04	1.92E−04	1.4%
14	3	11	−	13	2	12	−	2677.5600	1.87E−04	1.94E−04	−3.8%
30	2	28	+	29	1	29	+	2678.5441	1.51E−04	1.49E−04	1.1%
16	3	13	−	15	2	14	−	2678.9673	2.14E−04	2.25E−04	−5.3%
16	3	13	+	15	2	14	+	2679.0129	2.37E−04	2.40E−04	−1.1%
17	3	15	−	16	2	14	−	2679.4951	2.38E−04	2.39E−04	−0.2%
17	3	15	+	16	2	14	+	2679.5353	2.53E−04	2.53E−04	−0.3%
34	3	31	−	33	2	32	−	2690.5769	1.92E−04	1.90E−04	1.0%
34	3	31	+	33	2	32	+	2690.6017	1.85E−04	1.96E−04	−6.2%
11	4	8	+	10	3	7	+	2691.5808	1.39E−04	1.50E−04	−7.8%
36	3	33	−	35	2	34	−	2691.8208	1.55E−04	1.63E−04	−5.0%
36	3	33	+	35	2	34	+	2691.8455	1.59E−04	1.67E−04	−4.9%
12	4	8	−	11	3	9	−	2692.2220	1.48E−04	1.54E−04	−4.2%
12	4	8	+	11	3	9	+	2692.3049	1.64E−04	1.68E−04	−2.3%
13	4	10	+	12	3	9	+	2693.0189	1.77E−04	1.85E−04	−4.6%
38	3	35	−	37	2	36	−	2693.0741	1.29E−04	1.36E−04	−5.5%
38	3	35	+	37	2	36	+	2693.0988	1.37E−04	1.39E−04	−1.3%
14	4	10	−	13	3	11	−	2693.6526	1.71E−04	1.88E−04	−9.6%
16	4	12	−	15	3	13	−	2695.0419	2.09E−04	2.19E−04	−4.9%
34	4	30	+	33	3	31	+	2705.7356	2.52E−04	2.06E−04	18.0%
13	5	9	−	12	4	8	−	2709.1637	1.46E−04	1.49E−04	−2.5%
14	5	9	−	13	4	10	−	2709.8747	1.78E−04	1.65E−04	7.3%
15	5	11	−	14	4	10	−	2710.5753	1.73E−04	1.80E−04	−3.7%
15	5	11	+	14	4	10	+	2710.6598	1.95E−04	1.92E−04	1.5%
23	5	19	+	22	4	18	+	2715.8678	2.76E−04	2.67E−04	3.2%
24	5	19	−	23	4	20	−	2716.4215	2.57E−04	2.57E−04	−0.1%
24	5	19	+	23	4	20	+	2716.4741	2.72E−04	2.68E−04	1.6%
25	5	21	−	24	4	20	−	2717.0196	2.51E−04	2.57E−04	−2.2%
36	5	31	+	35	4	32	+	2722.9499	1.64E−04	1.67E−04	−1.7%

(*continued*)

Table 6. Continued.

N′	K'_a	K'_c	J′	N″	K''_a	K''_c	J″	Sigma	Int_obs	Int_calc	O–C in %
38	5	33	+	37	4	34	+	2723.8834	1.46E−04	1.42E−04	2.9%
39	5	35	−	38	4	34	−	2724.2951	1.25E−04	1.26E−04	−0.8%
39	5	35	+	38	4	34	+	2724.3236	1.36E−04	1.29E−04	4.9%
14	6	8	−	13	5	9	−	2726.1186	1.34E−04	1.32E−04	1.5%
16	6	10	+	15	5	11	+	2727.6044	1.59E−04	1.68E−04	−5.8%
17	6	12	+	16	5	11	+	2728.2794	1.78E−04	1.80E−04	−0.9%
20	6	14	−	19	5	15	−	2730.1687	2.13E−04	1.98E−04	7.0%
20	6	14	+	19	5	15	+	2730.2455	2.20E−04	2.08E−04	5.6%
30	6	24	−	29	5	25	−	2736.1019	2.04E−04	1.96E−04	4.3%
30	6	24	+	29	5	25	+	2736.1521	2.15E−04	2.02E−04	5.8%
37	6	32	+	36	5	31	+	2739.6822	1.44E−04	1.33E−04	7.6%
38	6	32	−	37	5	33	−	2740.1078	1.36E−04	1.19E−04	11.9%
16	7	9	−	15	6	10	−	2743.7004	1.15E−04	1.18E−04	−2.9%
17	7	11	−	16	6	10	−	2744.3793	1.34E−04	1.28E−04	4.2%
18	7	11	+	17	6	12	+	2745.1456	1.46E−04	1.45E−04	1.0%
23	7	17	−	22	6	16	−	2748.2362	1.82E−04	1.67E−04	8.3%
26	7	19	−	25	6	20	−	2750.0258	1.87E−04	1.69E−04	9.7%
32	7	25	−	31	6	26	−	2753.3272	1.50E−04	1.43E−04	4.4%
33	7	27	+	32	6	26	+	2753.8943	1.71E−04	1.40E−04	18.0%
36	7	29	+	35	6	30	+	2755.3691	1.37E−04	1.16E−04	15.6%
20	8	12	+	19	7	13	+	2762.5140	1.37E−04	1.15E−04	16.4%
30	8	22	+	29	7	23	+	2768.3592	1.36E−04	1.20E−04	11.6%
31	8	24	−	30	7	23	−	2768.8227	1.23E−04	1.12E−04	8.7%
31	8	24	+	30	7	23	+	2768.8874	1.45E−04	1.16E−04	20.1%
32	8	24	+	31	7	25	+	2769.4053	1.38E−04	1.11E−04	19.7%

In such conditions, R_L^U is written as

$$R_L^U = \left| \sum_{\nu';N'_0k'\gamma'} \sum_{N_0k\gamma} C^{\nu';J'N'K'_aK'_c}_{\nu';N'_0k'\gamma'} \times C^{0;JNK_aK_c}_{0;N_0k'\gamma} \times \left\langle N'_0k'SJ'\gamma'|^{\nu'0}\mu_Z^T|N_0kSJ\gamma \right\rangle \right|^2 . \quad (11)$$

The first difficulty that one has to face is to account correctly for the effects of the electron spin-rotation during the line intensity calculation. As usual, it is assumed here that the $^{\nu'0}\mu_Z^T$ transition moment operator of a given (ν')–(0,0,0) band 'acts' only as an 'N-type' rotational type coordinates. This means that we neglected, in the rotational expansion of $^{\nu'0}\mu_Z^T$, all terms involving spin-rotation operators.

Therefore, following the historical paper of Bowater *et al.* (see Eq. (37) in Ref.[25]), the following expression holds [3,34]:

$$\left\langle N'_0k'SJ'\gamma'|^{\nu'0}\mu_Z^T|N_0kSJ\gamma \right\rangle = (-1)^{N_0+S+J'+1}\sqrt{(2J+1)(2J'+1)} \begin{Bmatrix} J & 1 & J' \\ N'_0 & S & N_0 \end{Bmatrix} \ldots \times \left\langle N'_0k'\gamma'|^{\nu'0}\mu_Z^T|N_0k\gamma \right\rangle . \quad (12)$$

where {} represents the usual {6j} coefficient.

Finally; the $\left\langle N'_0k'\gamma'|^{\nu'0}\mu_Z^T|Nk\gamma \right\rangle$ matrix elements are computed using the method which is described for water vapour in Ref. [36]. In particular, we use the same expressions to deal with the centrifugal distortion effects.

$$^{\nu'0}\mu_Z^T = \sum_j {}^{\nu'0}\mu'_j \times {}^{\nu'}A_j \quad (13)$$

In Equation (13), $^{\nu'}A_j$ are symmetry-dependent rotational operators which are quoted in Table 7, while the $^{\nu'0}\mu'_j$ are numerical coefficients determined through the least squares fit performed on the experimental line intensities.

We note that the expression used here to account for the spin-rotation effects on NO_2 line intensities differs from the one quoted in several recent articles on NO_2.

Table 7. Transition moment constants for the $2\nu_1$ and $\nu_1+\nu_3$ band of NO_2.

	Value in Debye[a]	
	(2,0,0)–(0,0,0)[b]	Ref.
φ_x	$0.1671(6) \times 10^{-2}$	This Work
$\{\varphi_z, iN_y\}$	$0.5576(1) \times 10^{-4}$	This Work
$\{\varphi_z, N_xN_z + N_zN_x\}$	$-0.39454(3) \times 10^{-5}$	This Work
	(1,0,1)–(0,0,0)	
φ_z	0.496895×10^{-1}	[7]
$1/2[\{\varphi_x, iN_y\} - \{i\varphi_y, N_x\}]$	-0.991×10^{-5}	[7]
$1/2[\{\varphi_x, iN_y\} + \{i\varphi_y, N_x\}]$	-0.2897×10^{-4}	[7]

[a] 1 Debye = 3.33564×10^{-30} C·m. φ_x, φ_y and φ_z are the abbreviated notation for the Φ_{Zx}, Φ_{Zy} and Φ_{Zz}direction cosines between the Z-fixed and the x, y, z molecular fixed axes.

[b] The uncertainties quoted for in the (2,0,0)–(0,0,0) column are purely statistical errors, with poor physical meanings. Because of several experimental uncertainties a global systematic error of about ∼20% can affect these parameters.

Indeed, in Ref. [19,37–42], Equation (12) is re-written as

$$\left\langle N'_0 k' SJ'\gamma' |^{\nu' 0}\mu_Z^T | N_0 kSJ\gamma \right\rangle = g(N'_0, J', N_0, J)) \times \left\langle N'_0 k'\gamma' |^{\nu' 0}\mu_Z^T | Nk\gamma \right\rangle, \quad (14)$$

which is not correct, since they use the $g(J', N'_0, J, N_0)$ values tabulated in Table III of Ref. [43] as

$$g(J', N'_0, J, N_0) = \left((-1)^{N_0+S+J'+1} \sqrt{(2J+1)(2J'+1)} \times \begin{Bmatrix} J & 1 & J' \\ N'_0 & S & N_0 \end{Bmatrix} \right)^2. \quad (15)$$

Note also that the right hand side of Equation (12) also includes a phase factor $(-1)^{N_0+S+J'+1}$, which was not accounted for, in Equation (14).

For the spectral region under study, the vibrational expansion of the transition moment (see Equation (10)) involves, in principle, the (six) transition moment operators of the $2\nu_1$, $\nu_1+2\nu_2$, $\nu_1+\nu_3$, $4\nu_2$, $2\nu_2+\nu_3$ and $2\nu_3$ bands. However, to compute the line intensities of the $2\nu_1$, $\nu_1+2\nu_2$, and $\nu_1+\nu_3$ bands the calculation can be simplified. The $\nu_1+\nu_3$ band is, by far, the strongest band in this spectral region, and only the (1,0,1) energy levels are affected by the vibration–rotation resonances coupling the {(2,0,0), (1,2,0), (1,0,1)} and {(0,4,0), (0,2,1), (0,0,2)} blocks of interacting states. Since these resonances remain rather weak, it is clear that these inter-blocks resonances have a negligible impact on the $2\nu_1$, $\nu_1+2\nu_2$ and $\nu_1+\nu_3$ line intensities.

As far as the $\nu_1+\nu_3$ band is concerned, a good set of line intensity parameters already exists which were obtained from experimental line intensities during the detailed investigation performed for this band by Mandin *et al.* [7]. During that work, it appeared, and this is confirmed here, that the dark $\nu_1+2\nu_2$ band borrows all its intensity from the $\nu_1+\nu_3$ band through Coriolis resonances. It is also obvious that an intensity transfer exists between the strong $\nu_1+\nu_3$ band and the very weak $2\nu_1$ band. In such conditions, the expansion of the transition moment operator to be used for line intensities in the 2800–2950 cm^{-1} spectral region takes a form which is more simple than in Equation (10):

$$\mu'_Z = |0\rangle \langle (2,0,0)|^{200,0}\mu'_Z + |0\rangle \langle (1,0,1)|^{101,0}\mu'_Z. \quad (16)$$

Indeed, as mentioned previously we assume a zero value ($^{120,0}\mu'_Z = 0$) for the transition moment operator of the $\nu_1+2\nu_2$ dark band. Therefore, up to now, the only missing information concerns the transition operator of the very weak $2\nu_1$ band.

5.3. Line intensity calculations

In a preliminary test we included in a common fit the 93 experimental line intensities of $2\nu_1$ achieved during the present study, together with the existing (1047) individual $\nu_1+\nu_3$ line intensities of the literature [7] to determine the expansions of the $\nu_1+\nu_3$ and $2\nu_1$ bands. It turned out that the expansion of $^{101,0}\mu'_Z$ did not change notably as compared to what was obtained in Ref. [7]. This confirms that the $\nu_1+\nu_3$ line intensities are not significantly affected by the resonances coupling $\nu_1+\nu_3$ and $2\nu_1$.

Therefore, the final least squares fit computation was performed using only the 93 experimental line intensities of the $2\nu_1$ band. During this calculation, $^{101,0}\mu'_Z$ operator was maintained fixed at its form determined in Ref. [7], and the $^{101,0}\mu'_j$ parameters appearing in the expansion of $^{101,0}\mu'_Z$ (see Equation (15)) were adjusted. The final expansions of the $\nu_1+\nu_3$ and $2\nu_1$ transition moment operators are given in Table 7. It is important to mention that the uncertainties quoted for the $^{101,0}\mu'_j$ parameters in this table are only statistical errors, with a poor physical meaning. Indeed, considering the uncertainties associated:

- the NO_2 partial pressure during the recording of the spectrum (about 2%)
- the absorption due to N_2O_4 in the spectral range of the $2\nu_1$ band of NO_2.
- only one FTS spectrum was used for the retrieval.

One can estimate an overall uncertainty at about 20% (no more) for all the $^{200,0}\mu'_j$ parameters.

6. Synthetic spectrum: line position, line intensity and line shape parameters

6.1. Line positions and intensities

Using the vibrational energies and rotational, spin-rotational, and coupling constants given in Table 4 for the {(2,0,0), (1,2,0), (1,0,1)}, (0,4,0), (0,2,1), (0,0,2)} upper resonating vibrational states and in Ref. [18] for the (0,0,0) state, a comprehensive list of line positions were generated for the $2\nu_1$, $\nu_1+2\nu_2$ and $\nu_1+\nu_3$ band of NO_2. The corresponding line intensities were computed using $^{200,0}\mu'_j$ and $^{101,0}\mu'_j$ transition moment operator which are described in Table 7. The calculations were performed at 296 K for a natural nitrogen dioxide sample and with an intensity cut-off of 0.5×10^{-25} cm^{-1}/(molecule cm^{-2}).

The results of this intensity calculation, in terms of frequency ranges and of maximum N and K_a values in the upper states, are given in Table 8.

Table 8. Results of the line intensity calculations (for a natural sample of NO_2).

	Number	S_min	S_max	I_max	Int_Tot	*N* Max	K_a max
This work							
$2\nu_1$	5982	2457.95	2921.80	0.23d−22	0.84D−20	71	13
$\nu_1+2\nu_2$	1531	2740.02	2977.47	0.53d−23	0.83D−21	77	7
$\nu_1+\nu_3$	8731	2688.75	3148.79	0.66d−20	0.287d−17	80	15
HITEMP [17]							
$2\nu_1$	9315	2402.35	2870.30	0.56d−23	0.30D−20	99	15
$\nu_1+2\nu_2$	1856	2665.96	2963.42	0.67d−23	0.10D−20	99	7
$\nu_1+\nu_3$	10223	2679.94	3074.15	0.66d−20	0.287D−17	99	15
HITRAN [13] or previous GEISA [14]							
$\nu_1+2\nu_2$	890	2768.27	2963.42	0.67d−23	0.962E−21	70	7
$\nu_1+\nu_3$	6708	2719.06	3074.15	0.66d−20	0.287D−17	70	13

Note: The band intensities are in 10^{-20} $cm^{-1}/(molecules.cm^{-2})$ at 296 K. Line intensity cut-off: $k_{\tilde{\nu}}^{N}(296\,K) \geq 0.500^{-25}$ $cm^{-1}/(molecules.cm^{-2})$.

This table also compares the lists available for these cold bands in the HITRAN [13] or HITEMP [17] databases. One can notice that the present calculation leads to a computed $2\nu_1$ band intensity value which is larger by a factor of $\sim$2.8 as compared to HITEMP. This is quite reasonable, owing that (i) up to now nothing was known concerning the $2\nu_1$ intensities (ii) the difficulties (experimental and theoretical) for getting intensities for this weak band.

6.2. Line shape parameters

Our linelist includes also line broadening parameters. The most complete set of accurate line shape parameters, which includes air-broadening linewidths and their *n*-temperature dependences, and pressure lineshift for the ν_3 band of NO_2, were measured by Benner *et al.* [44]. As far as the air-broadening linewidths and its associated *n*-temperature dependences are concerned, these ν_3 band results are also usable for other vibrational bands. In our linelist, we used the polynomial expansion in 'm' ($m = N_{lower}$ for P or Q lines, and $m = N_{upper}$ for lines) proposed in Ref. [44]. On the other hand, in our list, all pressure line shifts are set at the (default) zero value. Indeed, the pressure shift values achieved for the ν_3 band of NO_2 [44] cannot be applied to any other vibrational band of NO_2 and the vibrational scaling factor which was applied for the pressure shift in the HITEMP database (see Eq. 8 of Ref. [17]) does not have any physical meaning [45]. Finally the default value $\gamma_{Self} = 0.095\,cm^{-1}/atm$ [4] was set up for the self-broadening parameters.

6.3. Inclusion in the GEISA database

This list of line positions, line intensities and line shape parameters for the $2\nu_1$, $\nu_1+2\nu_2$ and $\nu_1+\nu_3$ band of NO_2, which was prepared in a format suitable for public access databases, is now included in the GEISA database (https://geisa.aeris-data.fr/) [14,46].

7. Validation with the experimental spectrum

The overview of the 2520–3000 cm^{-1} spectral region is presented in Figure 1. For the cold bands, there exists an overall very good agreement between the experimental and calculated spectra of the $2\nu_1$ band and $\nu_1+\nu_3$ bands of $^{14}N^{16}O_2$.

Figure 2 shows the 2790–2830 cm^{-1} region which corresponds to the P-branch of the $\nu_1+\nu_3$ band and its associated hot bands, together with several lines from the $2\nu_1$. Figure 3 provides a detailed view of the same figure in the 2815 cm^{-1} region. It is clear that HITEMP cannot help for the analysis of the $2\nu_1$ band. Several spin-components doublets of the dark $\nu_1+2\nu_2$ band are also observable in this spectral region.

Figure 4 gives the overall structure of the $2\nu_1$ band. Clearly the general line intensity pattern is quite different from the 'classical' B-type, as described by the HITEMP linelist.

This is even more obvious in Figure 5, which provides a detailed view of the PQ7-branch of the $2\nu_1$ band in the 2537 cm^{-1} spectral region.

Figure 6 gives a portion of the $^{Q}Q_{12}$-branch of the $\nu_1+\nu_3$ band in the 2884 cm^{-1} spectral region. The comparison of the calculations performed using the present linelist and the HITRAN, GEISA or HITEMP to the observed spectrum shows the progress achieved during this work.

Figures 7–10 presents several portions of the R-branch of the $\nu_1+\nu_3$ band in the 2924, 2926.7 and 2938.6 cm^{-1} spectral regions, respectively. Due to local resonances, several spin-components doublets of the dark $\nu_1+2\nu_2$ band are identified for the first time in Figures 7, 9 and 10. Figure 8 shows that the $K_a = 8$ series of the $\nu_1+\nu_3$ band are shifted relative to their positions in HITRAN or GEISA. This is because of the local C-type Coriolis

resonance coupling the $K_a = 8$ energy levels of (1,0,1) with those in $K'_a = 5$ values of the (0,0,2) state were not accounted for during our previous investigation of the $\nu_1 + \nu_3$ band [7].

8. Conclusion

A new analysis of the $2\nu_1$ band and an extension of a previous FTS investigation of the $\nu_1 + \nu_3$ band of $^{14}N^{16}O_2$ has been achieved using high-resolution Fourier transform spectrum recorded in the 2400–3100 cm^{-1} spectral range. For the first time, several transitions could be identified for the dark $\nu_1 + 2\nu_2$ band. Together with those achieved during a 1997 study for the $\nu_1 + \nu_3$ band, the results of this analysis were combined with those achieved in 1996 for the $2\nu_2 + \nu_3$, $4\nu_2$ and $2\nu_3$ bands, using the same technique. The effective Hamiltonian matrix used for the energy level modelling accounts for numerous vibration–rotation resonances between states belonging to the {(2,0,0), (1,2,0), (1,0,1)} and {(0,4,0), (0,2,1), (0,0,2)} blocks of interacting states together with electron spin-rotation interactions within each vibrational state. The fit of the 93 parameters of the effective Hamiltonian allowed reproducing 3357 spin-rotation energy levels with an *rms* of 0.9×10^{-3} cm^{-1} for the (meas.-calc.) deviations. About ninety individual line intensities were measured for the $2\nu_1$ band, leading to the first set of intensity parameters for this weak band. Finally, a comprehensive list of line positions, intensities and line broadening parameters has been generated for the $2\nu_1$, $\nu_1 + 2\nu_2$ and $\nu_1 + \nu_3$ bands of $^{14}N^{16}O_2$ and is now included in the GEISA database (https://geisa.aeris-data.fr/).

Acknowledgements

The authors are very grateful to Dr Jean-Marie Flaud and Dr Johannes Orphal for their strong encouragements and suggestions during the pursuit of this work.

Disclosure statement

Q7 No potential conflict of interest was reported by the authors.

Funding

Q3 This work was financially supported by the French national program LEFE ('Les Enveloppes Fluides et l'Environnement') Q4 of the CNRS.

References

[1] A. Perrin, J.-M. Flaud, C. Camy-Peyret, B. Carli and M. Carlotti, Mol. Phys. **63**, 791–910 (1988).
[2] A. Perrin, J.-M. Flaud, C. Camy-Peyret, A. Goldman, J.F. Murcray, R.D. Blatherwick and C.P. Rinsland, J. Mol. Spectrosc. **160**, 456 (1993).
[3] A. Perrin, J.-M. Flaud, C. Camy-Peyret, A.-M. Vasserot, G. Guelachvili, A. Goldman, F.J. Murcray and R.D. Blatherwick, J. Mol. Spectrosc. **154**, 391 (1992).
[4] A. Perrin, J.M. Flaud, C. Camy-Peyret, D. Hurtmans, M. Herman and G. Guelachvili, J. Mol. Spectrosc. **168**, 54 (1994).
[5] A. Perrin, J.-M. Flaud, C. Camy-Peyret, D. Hurtmans and M. Herman, J. Mol. Spectrosc. **177**, 58 (1996).
[6] F. Gueye, F. Kwabia Tchana, X. Landsheere and A. Perrin, J. Quant. Spectrosc. Radiat. Transf. **138**, 60 (2014).
[7] J.-Y. Mandin, V. Dana, A. Perrin, J.-M. Flaud, C. Camy-Peyret, L. Régalia and A. Barbe, J. Mol. Spectrosc. **181**, 379 (1997).
[8] T.M. Stephen, A. Goldman, A. Perrin, J.-M. Flaud, F. Keller and C.P. Rinsland, J. Mol. Spectrosc. **201**, 134 (2000).
[9] S. Miljanic, A. Perrin, J. Orphal, C.E. Fellows and P. Chelin, J. Mol. Spectrosc. **251**, 9 (2008).
[10] A. Cabana, M. Laurin, W.J. Lafferty and R.L. Sams, Can. J. Phys. **53**, 1902 (1975).
[11] W.T. Raynes, J. Chem. Phys. **41**, 3020 (1964).
[12] V. Dana, J.-Y. Mandin, M.-Y. Allout, A. Perrin, L. Regalia, A. Barbe, J.-J. Plateaux and X. Thomas, J. Quant. Spectrosc. Radiat. Transf. **57**, 445 (1997).
[13] I.E. Gordon, L.S. Rothman, C. Hill, R.V. Kochanov, Y. Tana, P.F. Bernath, M. Birk, V. Boudon, A. Campargue, K.V. Chance, B.J. Drouin, J.-M. Flaud, R.R. Gamache, J.T. Hodges, D. Jacquemart, V.I. Perevalov, A. Perrin, K.P. Shine, M.A. Smith, J. Tennyson, G.C. Toon, H. Tran, V.G. Tyuterev, A. Barbe, A.G. Császár, V.M. Devi, T. Furtenbacher, J.J. Harrison, J.M. Hartmann, A. Jolly, T.J. Johnson, T. Karman, I. Kleiner, A.A. Kyuberis, J. Loos, O.M. Lyulin, S.T. Massie, S.N. Mikhailenko, N. Moazzen-Ahmadi, H. Müller, O.V. Naumenko, A.V. Nikitin, O.L. Polyansky, M. Rey, M. Rotger, S.W. Sharpe, K. Sung, E. Starikova, S.A. Tashkun, J. Vander Auwera, G. Wagner, J. Wilzewski, P. Wcisło, S. Yuh and E.J. Zak, J. Quant. Spectrosc. Radiat. Transf. **203**, 3–69 (2017).
[14] N. Jacquinet-Husson, R. Armante, N.A. Scott, A. Chédin, L. Crépeau, C. Boutammine, A. Bouhdaoui, C. Crevoisier, V. Capelle, C. Boonne, N. Poulet-Crovisier, A. Barbe, D.C. Benner, V. Boudon, L.R. Brown, J. Buldyreva, A. Campargue, L.H. Coudert, V.M. Devi, M.J. Down, B.J. Drouin, A. Fayt, C. Fittschen, J.-M. Flaud, R.R. Gamache, J.J. Harrison, C. Hill, Ø Hodnebrog, S.M. Hu, D. Jacquemart, A. Jolly, E. Jiménez, N. Lavrentieva, A.W. Liu, L. Lodi, O.M. Lyulin, S.T. Massie, S. Mikhailenko, H.S.P. Müller, O.V. Naumenko, A. Nikitin, C.J. Nielsen, J. Orphal, V. Perevalov, A. Perrin, E. Polovtseva, A. Predoi-Cross, M. Rotger, A.A. Ruth, Y. Shanshan, K. Sung, S. Tashkun, J. Tennyson, V.G. Tyuterev, J. Vander Auwera, B. Voronin and A. Makie, J. Mol. Spectrosc. **327**, 31–72 (2016).
[15] S. Miljanic, A. Perrin and J. Orphal, J. Mol. Spectrosc. **242**, 176–181 (2007).
[16] L.S. Rothman, I.E. Gordon, R.J. Barber, H. Dothe, R.R. Gamache, A. Goldman, V. Perevalov, S.A. Tashkun and J. Tennyson, J. Quant. Spectrosc. Radiat. Transf. **111**, 2139 (2010).

[17] R.J. Hargreaves, I.E. Gordon, L.S. Rothman, S.A. Tashkun, V.I. Perevalov, A.A. Lukashevskaya, S.N. Yurchenko, J. Tennyson and H.S.P. Müller, J. Quant. Spectrosc. Radiat. Transf**.** **232**, 35 (2019).
[18] A.A. Lukashevskaya, O.M. Lyulin, A. Perrin and V.I. Perevalov, Atmospheric and Oceanic Optics. **28**, 216 (2015).
[19] A.A. Lukashevskaya, N.N. Lavrentieva, A.C. Dudaryonok and V.I. Perevalov, J. Quant. Spectrosc. Radiat. Transf. **184**, 205 (2016); *ibid.***202**, 37 (2017).
[20] S. Reymond-Laruinaz, M. Faye, V. Boudon, D. Doizi and L. Manceron, J. Mol. Spectrosc. **336**, 29 (2017).
[21] K. Schofield, J. Phys. Chem. Ref. Data. **2**, 25 (1973).
[22] F. Mélen, F. Pokorni and M. Herman, Chem. Phys. Letters. **194**, 181 (1992).
[23] N. Semmoud-Monnanteuil, J.-M. Colmont, A. Perrin, J.-M. Flaud and C. Camy-Peyret, J. Mol. Spectrosc. **134**, 176 (1989).
[24] J.K.G. Watson, in *Vibrational Spectra and Structure*, edited by J.R. Durig (1977), Chap 1, Vol. 6, A Series of Advances, pp. 1–89.
[25] I.C. Bowater, J.M. Brown and A. Carrington, Proc. B. Soc. Lond. A. **333**, 265 (1973).
[26] A. Delon and R. Jost, J. Chem. Phys. **95**, 5686 (1991).
[27] T.J. Johnson, R.L. Sams and S.W. Sharpe, in *Chemical and Biological Point Sensors for Homeland Defense*, edited by A.J. Sedlacek III, R. Colton and T. Vo-Dinh (Bellingham, WA: SPIE, 2004), 5269, pp. 159–167, PNNL-SA-39521. doi:10.1117/12.515604.
[28] Y. Attafi, S. Galalou, H. Aroui, F. Kwabia Tchana, J. Vander Auwera, A. Ben Hassen, A. Perrin, L. Manceron and D. Doizi, J. Quant. Spectrosc. Radiat. Transf. **239**, 106679 (2019).
[29] Y. Attafi, A. Ben Hassen, H. Aroui, F. Kwabia Tchana, L. Manceron, D. Doizi, J. Vander Auwera and A. Perrin, J. Quant. Spectrosc. Radiat. Transf. **231**, 1 (2019).
[30] F. Kwabia Tchana, J.-M. Flaud, W.J. Lafferty and M. Ngom, Mol. Phys. **112**, 1633 (2014).
[31] F. Kwabia Tchana, M. Ngom, A. Perrin, J.-M. Flaud, W.J. Lafferty, S.A. Ndiaye and E.A. Ngom, J. Mol. Spectrosc. **292**, 1 (2013).
[32] A. Ben Hassen, F. Kwabia Tchana, J.-M. Flaud, W.J. Lafferty, X. Landsheere and H. Aroui, J. Mol. Spectrosc. **282**, 30 (2012).
[33] V. Dana and J.Y. Mandin, J. Quant. Spectrosc. Radiat. Transf. **48**, 725 (1992).
[34] A. Perrin, M. Ndao and L. Manceron, J. Quant. Spectrosc. Radiat. Transf. **200**, 12 (2017).
[35] P. De Bievre, N.E. Holden and I.L. Barnes, J. Phys. Chem. Ref. Data. **13**, 809 (1984).
[36] J.-M. Flaud and C. Camy-Peyret, J. Mol. Spectrosc. **55**, 278 (1975).
[37] A.A. Lukashevskaya, O.V. Naumenko, D. Mondelain, S. Kassi and A. Campargue, J. Quant. Spectrosc. Rad. Transf. **177**, 225 (2016).
[38] A.A. Lukashevskaya, O.V. Naumenko, S. Kassi and A. Campargue, J. Mol. Spectrosc. **338**, 91 (2017).
[39] A.A. Lukashevskaya, S. Kassi, A. Campargue and V.I. Perevalov, J. Quant. Spectrosc. Rad. Transf. **200**, 17 (2017).
[40] A.A. Lukashevskaya, S. Kassi, A. Campargue and V.I. Perevalov, J. Quant. Spectrosc. Rad. Transf. **202**, 302 (2017).
[41] A.A. Lukashevskaya, D. Mondelain, A. Campargue and V.I. Perevalov, J. Quant. Spectrosc. Rad. Transf. **219**, 393 (2018).
[42] O.V. Naumenko, A.A. Lukashevskaya, S. Kassi, S. Beguier and A. Campargue, J. Quant. Spectrosc. Rad. Transf. **232**, 146 (2019).
[43] V. Malathy Devi, P.P. Das, A. Bano, K. Narahari Rao, J.-M. Flaud, C. Camy-Peyret and J.P. Chevillard, J. Mol. Spectrosc. **88**, 251 (1981).
[44] D. Chris Benner, T.A. Blake, L.R. Brown, V. Malathy Devi, M.A.H. Smith and R.A. Toth, J. Mol. Spectrosc. **228**, 593 (2004).
[45] J.M. Hartmann, private communication.
[46] R. Armante, N. Scott, C. Crevoisier, V. Capelle, L. Crepeau, N. Jacquinet and A. Chédin, J. Mol. Spectrosc. **327**, 180 (2016).